

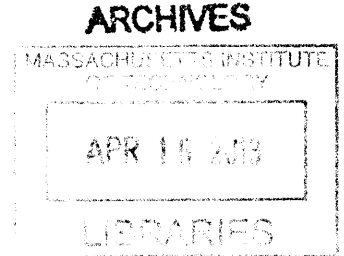
**Influence of topographic stress on rock fracture: A two-dimensional numerical model for arbitrary surface topography and comparisons with borehole observations**

by

Mirna I. Slim

B.S. Geology; American University of Beirut, 1998

M.S. Geology; Colorado School of Mines, 2007



Submitted to the department of Earth, Atmospheric and Planetary Sciences in partial fulfillment of the requirements for the degree of


Master of Science in Geophysics

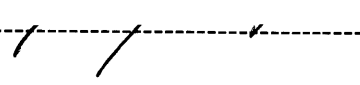
At the

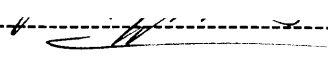
MASSACHUSETTS INSTITUTE OF TECHNOLOGY

February, 2013

© Massachusetts Institute of Technology 2013. All rights reserved.

Signature of Author: -----  
Department of Earth, Atmospheric, and Planetary Sciences  
December 17, 2012

Certified by: -----  
Taylor Perron  
Assistant Professor of Geology  
Thesis Supervisor

Accepted by: -----  
Robert van der Hilst  
Schlumberger Professor of Earth and Planetary Sciences  
Head of Dept. of Earth, Atmospheric and Planetary Sciences



# **Influence of topographic stress on rock fracture: A two-dimensional numerical model for arbitrary surface topography and comparisons with borehole observations**

by

Mirna I. Slim

Submitted to the department of Earth, Atmospheric and Planetary Sciences on December 17, 2012 in partial fulfillment of the requirements for the degree of Master of Science in Geophysics

## **Abstract**

Theoretical calculations indicate that topographic stresses in some landscapes may be large enough to fracture rocks, which in turn could influence slope stability, erosion rates, and bedrock hydrologic properties. These predictions typically have involved idealized topographic profiles, with few direct comparisons of predicted topographic stresses and observed fractures at specific field sites. I use a numerical model to calculate the stresses induced by measured topographic profiles and specified far-field tectonic stress. I compare the calculated stress field and potential shear fracture orientations with fracture abundance and fracture orientations observed in shallow boreholes. The model uses a boundary element method to calculate the stress distribution beneath an arbitrary topographic profile. When applied to topographic profiles extracted from a laser altimetry map of the Susquehanna/Shale Hills Critical Zone Observatory in central Pennsylvania, the model predicts considerable differences in depth profiles of stresses beneath ridgetops and valley floors. Using a representative value for the friction angle of shale, we calculate the minimum cohesion required to prevent shear failure,  $C_{\min}$ , as a proxy for the potential for fracturing or reactivation of existing fractures. We compare depth profiles of  $C_{\min}$  with structural analyses of image logs from four boreholes located on the valley floor, and find that fracture abundance declines sharply with depth in the uppermost 10 m of the boreholes, consistent with the modeled profile of  $C_{\min}$ . In contrast,  $C_{\min}$  increases with depth below ridgetops, suggesting that future analyses of ridgetop wells should observe a different trend in fracture abundance if topographic effects are indeed important. The numerical model used assumes the subsurface to be homogeneous and isotropic. The model-predicted fracture orientations do not reflect the scatter in fracture orientations seen in the wells. Thus, the present results support the hypothesis that topography can influence subsurface rock fracture patterns, suggest the imitation and reactivation of fractures of different generations, and provide a basis for further observational tests.

Thesis Supervisor: Taylor Perron

Title: Assistant Professor of Geology

## Acknowledgments

Many people have contributed to make my research at MIT possible and my time enjoyable. I would like to thank my advisor, Professor Taylor Perron for his guidance, revision, and comments on my work. I thank him for long and short sessions discussing results and approaches doing the work. Thank you for teaching me lots of things beyond the content of this thesis.

I thank Professor Brian Evans for introducing me, in his own way, to rock mechanics and his encouragement and support during the years I spent at MIT. I thank Dr. Mike Fehler for accepting to be on my committee and his comments on my work.

I thank Professor Steve Martel for sharing his BEM code to generate all the stress calculations, his time for discussing results, and his comments and insights writing and reviewing a manuscript based on this work. I thank Professor Kamini Singha and Tim White for sharing their borehole images allowing me to do the structural analysis. I thank Carole D. Johnson for answering questions on WellCAD, and Terryl Daniels for field assistance in collecting the OTV logs.

I thank Uli Mok for all his efforts making everything run on the 7<sup>th</sup> floor. Uli, I am thankful for all your help working in the rock mechanics lab and the many time you helped fixing and re-fixing lab equipments.

I thank Jok for his help in the machine shop and the tens of samples he helped coring and resizing.

I thank Professor Linn Hobbs, Shiahn Chen, Yong Zhang, and Patrick Boisvert with their help in the CMSE lab.

I thank Professor Samuel Bowring for his trust and help making few camping trips possible and affordable.

I feel grateful to Vicki McKenna, Carol Sprague, Brenda Carbone, Kerin Willis, and Jacqueline Taylor for help and assistance with many logistics and addressing many concerns and questions on a daily basis.

I thank Elan Pavlov for constructive discussions on image processing.

Finally, I want to express my appreciation to the friends I made during my years at MIT; Sudhish, Gabi, Amy, Armen, and Ahmed, I thank you all for a precious friendship, support, and simply always being there for me. Meeting you all partially explains why I ended up at MIT!

I deeply thank Roger and Dottie Marks, Anette and Roland Tang, Li, and Jack Ahern for making Sidney-Pacific (SP) a home away from home. I thank my SP friends (Ian, Chelsea, Tim, Pam, B, Alexandra, Jit, Adi, Pierre-Olivier, Mathieu, Hussam, Dina, Jeff, Farrah, Elan, Birendra, and Ozge) for making living at SP busy and fun.

I thank my family for the unconditional love and support. Thank you for your encouragement and patience while waiting for my return.

My apologies go to anyone who has helped me but whom I forgot to acknowledge.

# Contents

<b>Abstract.....</b>	<b>3</b>
<b>Acknowledgments .....</b>	<b>4</b>
<b>1. Introduction.....</b>	<b>11</b>
1.1 Motivation	11
1.2 Previous Work	12
1.3 Research Methodology and Summary	15
<b>2. Boundary Element Model for Stresses Induced by Arbitrary Topography .....</b>	<b>17</b>
2.1 Stresses in an Elastic Isotropic Medium	17
2.2 The Displacement Discontinuity Method (2dd)	19
2.3 Boundary Element Model Description	20
2.4 Failure Criterion and Cohesion at Failure	23
2.5 Influence of Topographic Aspect Ratio: Synthetic Calculations	26
<b>3. Application to the Shale Hills, Pennsylvania.....</b>	<b>29</b>
3.1 Site Description	29
3.2 Topography and Stress Calculations	31
3.3 Borehole Structural Analysis	34
3.4 Comparison of Fracture Abundance and Orientation with Modeled Topographic Stresses	38
<b>4. Discussion, Conclusions, and Implications .....</b>	<b>42</b>
4.1 Discussion	42
4.2 Summary and Conclusions	44

4.3 Implications and Recommendations for Future Work	46
<b>Appendix A: Comparison Between Analytical and Numerical Methods .....</b>	<b>47</b>
<b>Appendix B: Borehole Image Logs and Structural Data .....</b>	<b>53</b>
<b>References.....</b>	<b>73</b>

# List of Figures

Figure 1: The discontinuity displacement approach represents a crack by  $N$  elements..... 20

Figure 2: Conceptual illustration of Martel and Muller’s (2000) approach for calculating topographic stresses ..... 21

Figure 3: A gridded subsurface generated by the BEM code ..... 24

Figure 4: A Mohr circle ..... 25

Figure 5: Minimum Cohesion from the BEM under idealized sinusoidal topography..... 27

Figure 6: The stress map of central and eastern North America..... 30

Figure 7: (a) A shaded relief map of the Shale Hills study site and surroundings showing well locations and the trace of the cross-section used in this study. (b) Topographic profile studied ..... 32

Figure 8: Plots of (a)  $\sigma_{xx}$ , (b)  $\sigma_{yy}$ , (c)  $\tau_{max}$  and (d) Cohesion at failure obtained from the BEM..34

Figure 9: A section of an OBI log taken from CZMW 4..... 35

Figure 10: Stereonets showing arithmetic averages of the (a) fracture and (b) bedding plane orientations in the wells ..... 37

Figure 11: Depth profiles of cohesion-at-failure under (a) the ridgetop and (b) the valley floor. (c) Plot of fracture abundance in borehole image logs as a function of depth..... 39

Figure 12: Orientations of (a) principal stresses obtained from the BEM and (b) predicted fracture planes under the valley..... 40

Figure A-1: A comparison of analytical solutions and BEM solutions for a symmetric ridge .... 48

Figure A- 2: A comparison of analytical solutions and BEM solutions for a symmetric valley. 50

Figure A- 3: Cohesion-at-failure, under (a) the ridgetop in Figure A-1 and (b) the valley floor in Figure A-2..... 52



Figure B-1: Image log of CMZW 1 showing average traces of fracture and bedding planes ..... 56

Figure B-2: Image log of CMZW 2 showing average traces of fracture and bedding planes ..... 58

Figure B-3: Image log of CMZW 3 showing average traces of fracture and bedding planes ..... 61

Figure B-4: Image log of CMZW 4 showing average traces of fracture and bedding planes ..... 64

## List of Tables

Table B- 1: CMZW 1 bedding plane strike directions and dip angles.....	65
Table B- 2: CMZW 2 bedding plane strike directions and dip angles.....	66
Table B- 3: CMZW 3 bedding plane strike directions and dip angles.....	67
Table B- 4: CMZW 4 bedding plane strike directions and dip angles.....	68
Table B- 5: CMZW 1 fracture plane strike directions and dip angles .....	69
Table B- 6: CMZW 2 fracture plane strike directions and dip angles .....	70
Table B- 7: CMZW 3 fracture plane strike directions and dip angles .....	71
Table B- 8: CMZW 4 fracture plane strike directions and dip angles .....	72

# CHAPTER 1

## Introduction

### 1.1 Motivation

Gravitational and tectonic forces and rock mechanical properties determine the stress distribution in the Earth's crust (McNutt, 1980). Topographic effects can perturb the stress field and may cause the bedrock to fracture (McTigue and Mei, 1981; Savage et al., 1985; Miller and Dunne, 1996; Martel and Muller, 2000; Martel, 2011) or reactivate existing, healed/closed fractures if they are favorably oriented with respect to the principal stresses. Fractures in the shallow subsurface affect bulk rock strength and permeability, which should in turn affect rock erodibility, slope stability, infiltration capacity, and groundwater flow (Miller and Dunne, 1996; Morin and Savage, 2002; Morin et al., 2006). By altering permeability, topographic stresses could influence patterns of runoff and channel discharge. Also, topographically induced fracturing on a sufficiently large scale could lead to feedbacks between landscape evolution and rock fracturing and strength. For instance, the incision of river valleys may induce topographic stresses that promote rock fracture beneath valley floors, which could in turn accelerate valley incision (McTigue and Mei, 1981; Miller and Dunne, 1996; Molnar, 2004). Thus, rock fracturing associated with stresses generated by surface topography could substantially influence the development and evolution of landscapes.

Determining the extents to which these hypothesized effects actually occur requires a detailed understanding of the mechanisms that generate topographic stresses and fractures, and an evaluation of field evidence, including comparisons of observed rock fracture patterns with predicted topographic stresses. The lack of comparisons of predicted stresses with observed fractures is the main motivation for this thesis.

## 1.2 Previous Work

Early studies of topographic stresses focused on the effects of large-scale topography (tens of kilometers in horizontal extent) on the lithosphere at depths of kilometers or more (see review in McNutt, 1980). Holzhausen (1978) and McTigue and Mei (1981) were among the first to study the stress distribution immediately beneath local topographic features. Holzhausen (1978) examined an elastic medium with a simple sinusoidal surface using a perturbation method. McTigue and Mei (1981) also used a perturbation method but followed a Fourier transform approach (Sneddon, 1951). McTigue and Mei (1981) obtained approximate analytical solutions for the stress distribution in an elastic half-space with an irregularly shaped free surface and a gentle (0.1-0.25) regional slope. They showed that even if regional horizontal stresses are absent, topography induces local horizontal compressive stresses under ridgetops and local tensile stresses under valley floors, and that the effect of topography decreases with depth. They also showed that regional compressive stresses can induce local tensile stresses at topographic highs. Augustinus (1995) obtained the same results and showed that stress concentration on slopes made of low rock mass strength leads to failure that accelerates glacial erosion.

Exact analytical elastic solutions for the stress distribution under certain landforms were subsequently found by Savage et al. (1985) and Savage and Swolfs (1986). They used the analytical approach of Muskhelishvili (1953) to solve for the Airy's stress function in an isotropic medium. They calculated subsurface stresses under a class of idealized, symmetric valleys and ridges of various shapes described by a particular conformal coordinate mapping. Savage et al. (1985) calculated the effect of gravity in a laterally constrained medium. They showed that topographic stresses arising from gravitational effects alone are on the order of  $\rho gb$ , where  $\rho$  is the rock density,  $g$  is the acceleration of gravity, and  $b$  is ridge height or valley depth. Like Holzhausen (1978) and McTigue and Mei (1981), Savage et al. (1985) predict compressive stress under ridgetops, tensile stresses under valley floors, and stresses approaching those beneath a horizontal surface as depth increases. Savage and Swolfs (1986) additionally evaluated the effect of the tectonic stresses by calculating how topography perturbs an otherwise uniform compressive tectonic stress. They then superposed their solutions on those of Savage et al.

(1985) to obtain the stress distribution due to both tectonic and gravitational stresses. They demonstrated that topography reduces the effect of the regional compressive tectonic stress near ridge crests, even generating tension if the ridge is steep; that stresses in valleys decrease with shallower valley depth; that tectonic stresses are amplified in valleys; and that stresses under ridge crests persist even when surface slopes are small.

Savage et al. (1985) and Savage and Swolfs (1986) calculated subsurface stresses assuming the ratio  $k$  of the depth gradient of horizontal stress to the depth gradient of vertical stress was less than one. Miller and Dunne (1996) compiled reported crustal stress values from different geographic locations and concluded that in many places  $k$  exceeds unity. Noting that many of the reported stresses indicated high regional compressive tectonic stress, they used the approach of Savage et al. (1985) and Savage and Swolfs (1986) to calculate stresses for cases with  $k > 1$  and predicted the fracture patterns that would develop for various landforms and tectonic stress states. They substantiated the finding of Savage et al. (1985) that topographically induced stresses vary with landform shape (relief and steepness of valleys and ridges), and showed that tensile stresses might arise under ridgetops if  $k > 1$ .

Miller and Dunne (1996) discussed the implications of their fracture mode predictions for landscape evolution. Noting that elastic stresses scale with topographic relief, they proposed that fracturing might occur only if the topographic relief (ridge height above valley floor) is sufficiently high that the stresses exceed a Coulomb failure threshold. They also proposed a positive feedback between topographic stresses and landscape evolution, in which valley incision triggers fracturing in the valley floor, which then accelerates valley incision and further enhances the fracturing effect. Molnar (2004) revisited the examples discussed by both Savage et al. (1985) and Miller and Dunne (1996). He developed a framework for quantifying the positive feedback in sustaining a valley that Miller and Dunne (1996) proposed, and showed the dependence of stress concentration in a valley on its shape, especially the sharpness of the “V” at the valley axis.

Few studies were done to relate velocity measurements and sonic and image logs to

fracture abundance in the subsurface; Clarke and Burbank (2011) showed that the linear P-wave velocity gradient in the shallow multilayered subsurface is caused by non-linear decline in fracture density (a quantity relating the velocity of a horizontal layer at a certain depth, velocity of intact rocks, and velocity of the fracture filling material) and is independent of rock types. Clarke and Burbank (2011) state that the source of fractures can either be tectonic or geomorphic. They argue that tectonic fracturing produced a uniform/linear velocity and fracture density with depth in single-layered profiles and that the geomorphic processes focused within the near surface (0-15m) produce a depth-dependent or nonlinear fracture density change. Morin et al. (2006) processed sonic logs and borehole images to study the mechanical properties of fractured basalt and the permeability of subsurface fractures. They developed a finite element model that incorporates both topography and lithologic structure of the Annapolis Valley, Nova Scotia to calculate the subsurface stress distribution. They compared their calculated stress distribution with well fracture orientations. Martel (2011) predicted the areal distribution of sheeting joints in part of Yosemite National Park using an exact solution for the gradient in the normal stress perpendicular to the surface. He accounted for the site-specific topography but assumed the surface-parallel compressive stresses were constant. Observations of sheeting joints on short-wavelength domes, ridges, and saddles were consistent with the hypothesis that surface-parallel stresses and topography account for the formation of sheeting joints (Martel, 2011). An opening clearly exists for a more complete examination of the coupling between topography and stress state, the importance of this coupling at depth, and the combined impact on fractures at a specific site.

The aforementioned studies notwithstanding, few investigations have tested the predicted topographic stresses against observations from specific field sites. Savage and Morin (2002) and Morin and Savage (2002) applied the conformal mapping method of Savage et al. (1985) to both approximate the topography and predict the near-surface stresses at a study site in the Davis Mountains of Texas, and compared their predictions to the stresses inferred from borehole breakout orientations on acoustic image logs. They showed that breakout orientation appears to change with depth in a manner consistent with stress calculations. However, they did not attempt to compare predicted stresses with fracture patterns.

### **1.3 Research Methodology and Summary**

In this thesis, I implement a numerical method for calculating stresses beneath topographic profiles of arbitrary form, and compare predicted topographic stresses with fracture patterns mapped from shallow boreholes. I first employ the boundary element model of Martel and Muller (2000) to idealized synthetic profiles to illustrate effects of variable valley aspect ratio and tectonic stresses. Next, I calculate stresses along and beneath a high-resolution topographic profile across a valley in the Susquehanna/Shale Hills Critical Zone Observatory in central Pennsylvania. From the predicted stresses and mechanical properties of the rocks, I calculate a proxy for fracture susceptibility and compare that proxy to the fracture abundance distribution observed in optical logs of shallow (10-15 m) boreholes in the valley floor. I also calculate the shear fracture orientation that will develop in a homogeneous, isotropic medium. This allows me to test the hypothesis that topographic stresses contribute to the formation or reactivation of fractures in the shallow subsurface.

The model predicts a nonlinear trend of fracture abundance with depth in the shallow subsurface under the valley floor. This predicted trend reflects the combined effects of the ambient stress field and topography. It is in agreement with the fracture abundance observed in the wells and consistent with the hypothesis that topography affects the formation and activation of fractures in the shallow subsurface. Also, I compare model-predicted and observed fracture orientations. The fracture orientations observed in the wellbore agree with the horizontal stress directions reported (Zoback and Zoback, 1980 and 1989; Plumb and Cox, 1987; Heidbach et al., 2008). The fracture orientation predictions by the model does not reflect the different generations of fractures seen on image logs; the BEM fracture orientation prediction does not incorporate pre-existing fractures that can be reactivated as it assumes the subsurface to be homogeneous and isotropic. Finally, I comment on the depth to which topographic stress is likely to have a substantive influence on fracture development in the subsurface.

This study is one of very few that compares the predictions of a topographic stress model to actual observations in boreholes. My results show the relative importance of different factors that influence stresses beneath landforms; in particular, I show that tectonic stresses can mask the

influence of topography. The work described here provides a static snapshot of the predicted stress distribution beneath a particular topographic surface and its relationship to fractures observed in the shallow subsurface. This comparison is a necessary first step toward a more dynamic theory relating topographic stress and rock fracture to erosion and landscape evolution through time.



# CHAPTER 2

## Boundary Element Model for Stresses Induced by Arbitrary Topography

### 2.1 Stresses in an Elastic Isotropic Medium

A problem of elasticity is one where stresses and displacements at every location in a body of known shape and properties are determined. The body forces within the elastic medium and tractions and displacement along its boundaries must be known. The numerical method that will be described considers a finite body and will be compared to analytical solutions in infinite bodies. Therefore, far-field stresses and surface tractions need to be distinguished. An infinite body has no vertical ends and the notion of traction boundary conditions is not valid. Traction induce stresses within the body, and their effect decays away from the boundary/surface on which they act. On the other hand, far field stresses are specified within and throughout the body. They are different than the traction or stress boundary conditions; far-field stresses can represent horizontal normal stresses (e.g. tectonic stresses) in a body of infinite horizontal extent, stresses due to body forces (e.g. gravity), and stresses due to uniform horizontal normal stresses caused by uniform tractions on vertical ends of a finite body (Martel, 2000).

To determine the stress and displacement in a static medium, a set of equations of stress equilibrium (Equation 1) must be solved.

$$\frac{\partial \sigma_{xx}}{\partial x} + \frac{\partial \tau_{yx}}{\partial y} + \frac{\partial \tau_{zx}}{\partial z} + \rho F_x = 0 \quad (1a)$$

$$\frac{\partial \tau_{xy}}{\partial x} + \frac{\partial \sigma_{yy}}{\partial y} + \frac{\partial \tau_{zy}}{\partial z} + \rho F_y = 0 \quad (1b)$$

$$\frac{\partial \tau_{xz}}{\partial x} + \frac{\partial \tau_{yz}}{\partial y} + \frac{\partial \sigma_{zz}}{\partial z} + \rho F_z = 0 \quad (1c)$$

where  $\sigma_{ll}$  and  $\tau_{lm}$  ( $l, m = x, y, z$ ) are the components of the stress tensor denoted with two indices; the first indicates the direction of the outward unit normal vector of the plane on which the stress component is acting and the second indicates the components of the traction vector.  $\rho$  is density of the medium, and  $F(F_x, F_y, F_z)$  is the body force per unit mass. Equation 1 is general and contains no assumptions on the stress-strain behavior of the material constituting the medium (Jaeger et al., 2007). If stress-strain and strain-displacement relationships are specified in the medium, the Navier Equations that relate components of the displacement gradient and elastic properties of the medium to the body forces can be derived (Equations 5.81-5.83; Jaeger et al., 2007). The Navier equations are helpful to work with if the displacements at the medium boundaries are specified. However, most often, we have traction boundary conditions rather than displacements at the outer boundaries of the medium. Therefore, we need a strain compatibility equation (Equation 2).

$$2 \frac{\partial^2 \epsilon_{xy}}{\partial x \partial y} = \frac{\partial^2 \epsilon_{xx}}{\partial y^2} + \frac{\partial^2 \epsilon_{yy}}{\partial x^2} \quad (2)$$

With stress-strain relationships and expressing the body forces as gradients of the gravity potential function ( $V = -gz$ ), the stress components are expressed in terms of some function  $U$ , the Airy's stress function. The potential function  $V$  satisfies Laplace's equation; therefore  $U$  must satisfy the biharmonic equation (Equation 3). Solutions for Equation 3 are obtained by analytical solutions (Savage et al., 1985 and 1986) and yield displacement and stress distributions that satisfy both the equilibrium and compatibility equations.

$$\frac{\partial^4 U}{\partial x^4} + 2 \frac{\partial^4 U}{\partial x^2 \partial y^2} + \frac{\partial^4 U}{\partial y^4} = 0 \quad (3)$$

With a fixed, gravity-induced reference stress state, the ambient stresses in a laterally confined body in plane strain ( $\epsilon_{zz} = \epsilon_{zx} = \epsilon_{zy} = \epsilon_{xz} = \epsilon_{yz} = 0$ ) with a traction-free horizontal surface are:

$$\sigma_{xx} = \frac{\nu}{1 - \nu} \rho g y \quad (4a)$$

$$\sigma_{yy} = \rho g y \quad (4b)$$

$$\tau_{xy} = \tau_{yx} = 0, \quad (4c)$$

Where  $g$  is gravity and compressive stresses are treated as negative.

When a known point load is added to a horizontal surface, the stresses caused by this load and the displacement anywhere in the elastic half-space can be obtained (solving the Flamant's problem; Equations 3.1.1 and 3.1.2 in Crouch and Starfield, 1983). Using the principle of superposition, the stress distribution and displacements at any location in a finite elastic body (e.g. under an imaginary topographic surface) caused by a load of any shape (e.g. an overburden above a topographic surface) can be calculated.

## 2.2 The Displacement Discontinuity Method (2dd)

Crouch and Starfield's (1983) 2D displacement discontinuity method (2dd) is based on an analytical solution for a constant discontinuity displacement over a finite linear segment in an infinite, two-dimensional elastic solid. The method considers a crack in the solid (Figure 1) as being formed of  $N$  finite linear segments, each of which has opposite sides moving relative to one another. The displacement of each element is continuous everywhere except across the line segment itself, thus the name displacement discontinuity. The displacement discontinuity,  $D_i$  ( $D_x$ ,  $D_y$ ), is a vector whose magnitude is the difference between the displacements of the two sides of the crack. The displacements ( $u_x$ ,  $u_y$ ) and the stresses ( $\sigma_{xx}$ ,  $\sigma_{yy}$ , and  $\tau_{xy}$ ) due to the displacement discontinuity of each crack element can be computed (Equations 5.2.3 and 5.2.4 in Crouch and Starfield, 1983). The distribution of displacements along all crack elements that satisfies the traction boundary conditions of the problem and the stress distribution around the crack are calculated using the principle of superposition.

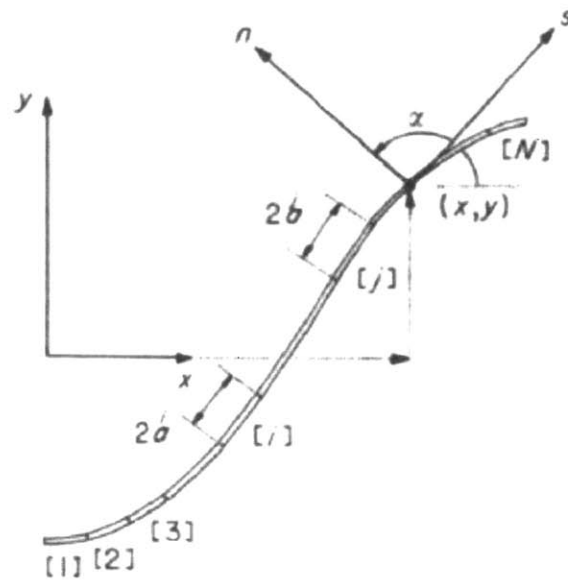


Figure 1: The discontinuity displacement approach represents a crack by  $N$  elements. The displacement of each element affects the stress distribution within the elastic body and the tractions on the rest of the crack elements.  $2a$  = crack element length.  $i$  and  $j$  are arbitrary crack-forming elements (reproduced from Crouch and Starfield, 1983).

### 2.3 Boundary Element Model Description

The need to study stresses induced by real topography, their interactions with variable tectonic stresses, and their effects on slope stability motivated Martel and Muller (2000) to develop a flexible numerical method that adopts a boundary element method (BEM) based on Crouch and Starfield's 2dd approach (1983). Martel and Muller (2000) treated a topographic surface as one half of a traction-free crack, with the opening of the crack corresponding to the removal of overburden that formed the topography (Figure 2).

They started by defining the ambient stress state under a horizontal surface (Equation 4) and used the ambient stress conditions away from the eventual topographic surface as boundary conditions for later scenarios (i.e. when the topography is introduced and the overburden removed). The justification for this approach is St. Venant's principle, which states that the addition or removal of a load by erosion introduces only local stresses and strains.

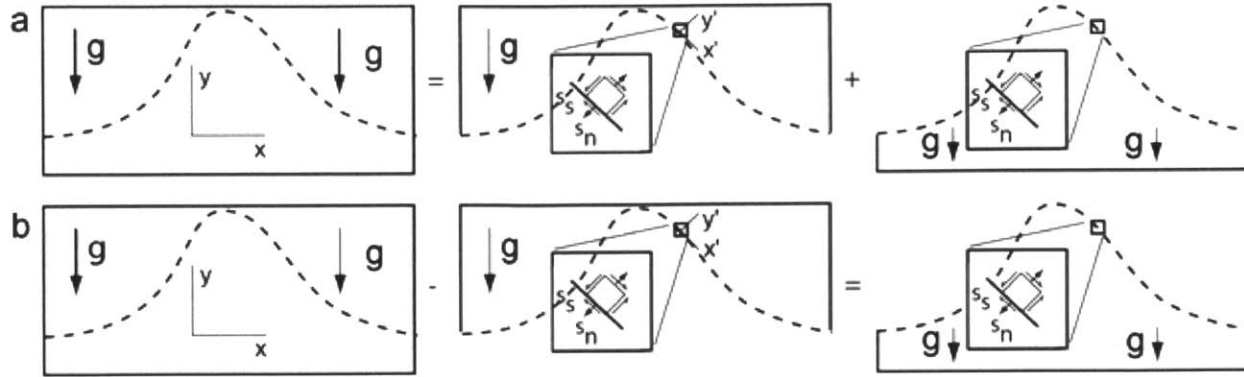


Figure 2: Conceptual illustration of Martel and Muller's (2000) approach for calculating topographic stresses. (a) The reference stress field (left) contains contributions from the stresses in the overburden above the land surface (middle) and stresses in the material below the land surface (right). (b) The stress field below the topographic surface is obtained by subtracting the effect of the overburden from the reference stress field. Different lengths of the arrow representing the gravity force do not imply a change in the magnitude of the force of gravity (reproduced from Martel and Muller, 2000).

With the shape of the topographic surface known, the topographic surface is viewed as an imaginary crack. The overburden above each of its elements is calculated. The tractions associated with the gravitational stresses due to the overburden above the (eventual) land surface (or crack) are then subtracted, leaving the land surface traction-free and the stresses beneath the surface altered from the ambient state (Figure 2).

The total stress field below the topographic surface is found by evaluating the perturbation to the stress field caused by the generation of the topography (i.e., by the erosion of overburden), and then superposing this perturbation on the fixed reference (ambient) stress state. The perturbation along the surface modeled by the crack is reflected by the change in normal and shear tractions that would arise due to erosion. Those traction changes, when superposed on the reference state, yield a traction-free surface. The traction changes also serve as boundary conditions along the crack for the stress perturbation solution and are stored in a matrix we refer to as  $[B_j]$ .

The traction perturbations on the walls of the crack used to model the topographic surface

induce relative displacement of the walls across each of the  $N$  crack elements. The displacements on the lower wall of the crack can be thought of as those experienced by the (eventual) ground surface in response to the removal of overburden. The relative displacement of the walls of any element (e.g. element  $i$ ; Figure 1) induces stresses everywhere else in the body, as well as tractions on the rest of the elements forming the surface/crack. The effects of unit relative displacements of all elements on a specific element and on any other observation point in the body are calculated and stored in influence-coefficient matrices  $[A_{ij}]$  and  $[A_{ij}^{obs}]$ , respectively.  $[A_{ij}]$  (length/stress) is a function of the elastic constants of the medium as well the spacing of boundary elements.

With the influence coefficient and boundary condition matrices calculated, the relative displacements at each element,  $[X_i]$ , are obtained by solving for the relative displacements of the crack walls needed to return the perturbed traction boundary-conditions using an inverse method (Martel and Muller, 2000):

$$[A_{ij}][X_i] = [B_j] \quad (5)$$

Once the relative displacements are solved for, the stress perturbations at the observation points beneath the land surface  $[\sigma_{ij}^{obs}]$  are calculated using a forward method:

$$[A_{ij}^{obs}][X_i] = [\sigma_{ij}^{obs}] \quad (6)$$

The resulting stress perturbation field is superposed on the reference (background) state to yield the stress field beneath a traction-free surface (Figure 2).

As reported by Martel and Muller (2000), the stresses calculated by the BEM for the symmetric topography studied by Savage et al. (1985) and Miller and Dunne (1996) compare very well with the analytical solutions of Savage et al. (1985). The BEM stresses are subject to numerical errors near the ends of the boundary elements (i.e., within approximately one element length below the ground surface), but show close agreement at greater depths (Appendix A).

Unlike the existing analytical solutions, the BEM can be used to calculate stresses beneath any topographic profile.

In our model working with topography, the  $x$ - and  $z$ -directions are horizontal (Figure 3). The positive  $y$ -direction points up, and  $y = 0$  is at the highest ridgetop in the topographic profile. Opposite ends of a profile are tapered to the same elevation (mid-way between the ridge top and valley bottom) so that there is no net topographic gradient across the modeling domain. With the ends of the modeled subsurface tapered to the same level and the same normal traction distribution applied to each end, the modeled body experiences no net lateral force and is in equilibrium.

#### 2.4 Failure Criterion and Cohesion at Failure

Given a stress field calculated with the BEM, we seek a quantity that represents the propensity for development of shear fractures or reactivation of existing ones. The Mohr-Coulomb failure criterion (Equation 7) defines the shear failure envelope of a material (Figure 4). In Figure 4,  $\sigma_1$  is the most compressive stress and  $\sigma_3$  is the least compressive stress. For a new shear fracture to form, the shear stress,  $\tau$ , acting on a plane must exceed the sum of the cohesive strength of the material,  $C_0$ , and the frictional resisting stresses, given by the term  $|\sigma_n|\tan\phi$ , where  $\phi$  is the internal friction angle and  $\sigma_n$  is the normal stress acting on the plane of weakness. The well-known graphical representation of the stress field in two dimensions is the Mohr circle (Figure 4). Shear fractures form if the Mohr circle touches the failure envelope. Failure occurs along planes with normal vectors that form angles  $\theta$  with the maximum compressive principal stress,  $\sigma_1$  (Figure 4). Pre-existing fractures (with normal vectors that form angles  $\theta_1$  and  $\theta_2$  with  $\sigma_1$ ) can be reactivated with a shear stress magnitude lower than that needed to initiate new fractures.

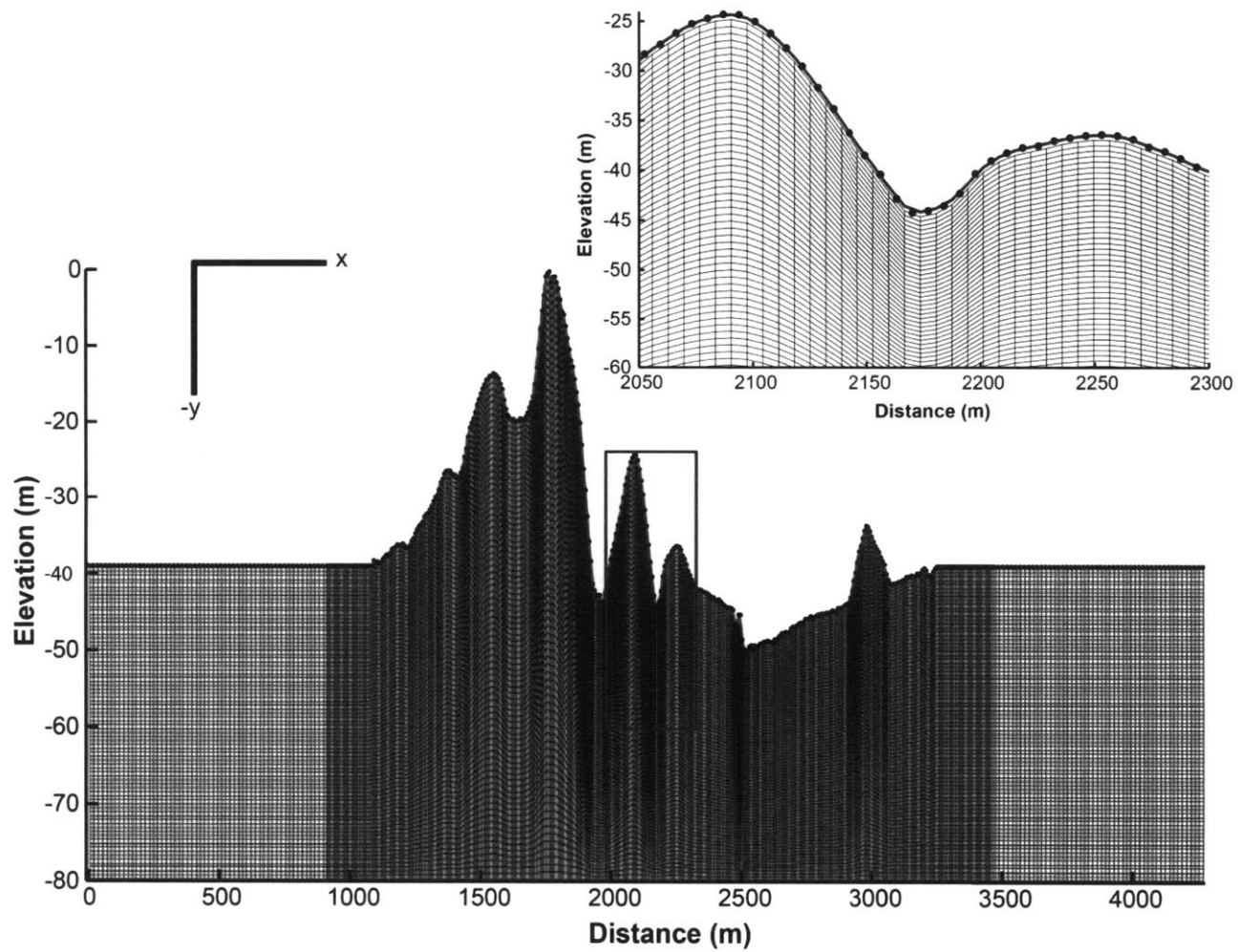


Figure 3: A gridded subsurface generated by the BEM code of Martel and Muller (2000) under an arbitrary topographic surface tapered at its ends. A magnified portion (blue box) of the topography shows the beginning and ends of surface elements with black circles. Grid intersections (beneath element midpoints) are observation points where stresses were calculated.



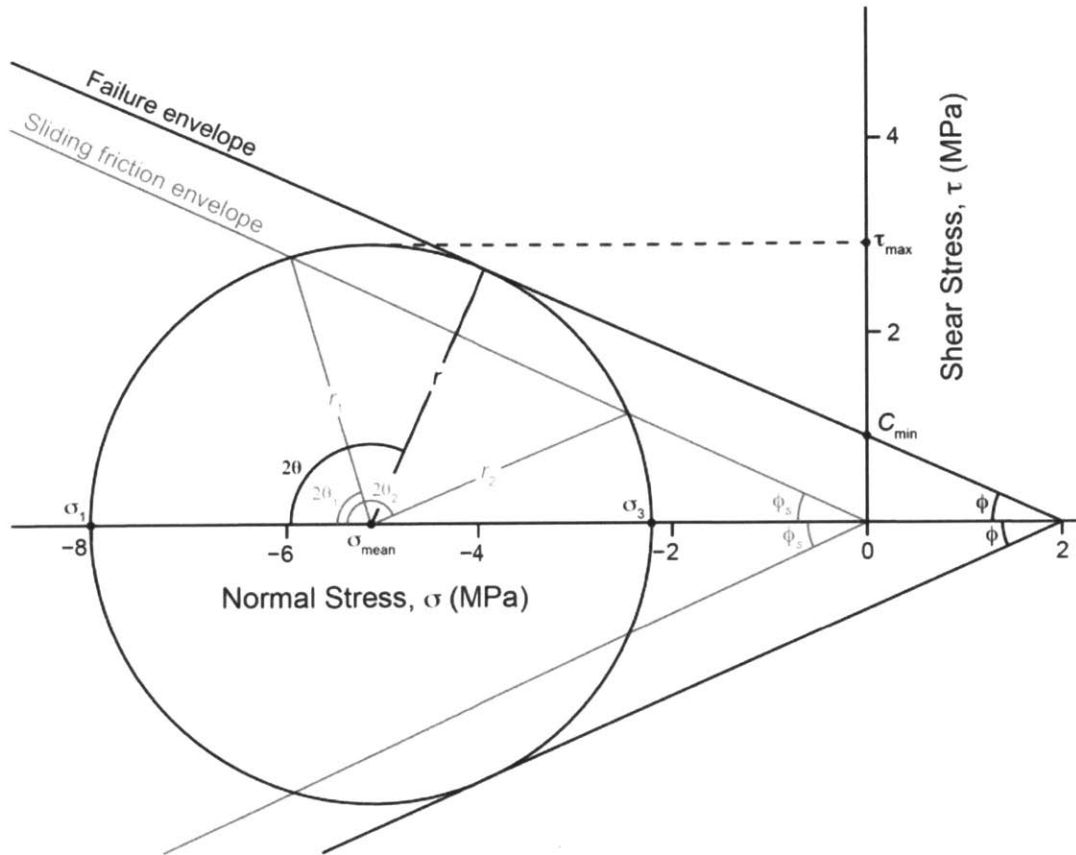


Figure 4: A Mohr circle drawn for a specific stress state defined by most compressive ( $\sigma_1$ ) and least compressive ( $\sigma_3$ ) principal stresses. The values of the mean stress,  $\sigma_{\text{mean}}$ , and the maximum shear stress,  $\tau_{\text{max}}$ , can be read from the normal and shear stress axes, respectively. Both the failure and sliding friction envelopes are drawn with a  $24^\circ$  angle of internal and sliding friction, respectively. The cohesion at failure ( $C_{\text{min}}$ ) is the cohesion for which the failure envelope is tangent to the Mohr circle.

$$|\tau| = |\sigma_n| \tan \phi + C_0 \quad (7)$$

The Mohr circle (Figure 4) represents the state of stress defined by the magnitudes of the maximum and minimum compressive stresses,  $\sigma_1$  and  $\sigma_3$ , at a specific point in the subsurface. The mean stress,  $\sigma_{\text{mean}}$ , and the maximum shear stress,  $\tau_{\text{max}}$ , are the center and radius of the Mohr circle, respectively, and are given by

$$\sigma_{\text{mean}} = \frac{|\sigma_1 + \sigma_3|}{2} \quad (8)$$

$$|\tau_{\text{max}}| = \frac{|\sigma_1 - \sigma_3|}{2} = \sqrt{\left(\frac{\sigma_{xx} - \sigma_{yy}}{2}\right)^2 + (\sigma_{xy})^2}, \quad (9)$$

where  $\sigma_{xx}$ ,  $\sigma_{yy}$ , and  $\sigma_{xy}$  are as defined above. Based on Mohr-Coulomb theory, the minimum cohesion needed to prevent the development of new shear fractures is (Jaeger et al., 2007; Figure 4):

$$C_{\text{min}} = \frac{|\tau_{\text{max}}| - |\sigma_{\text{mean}}| \sin \phi}{\cos \phi} = \frac{|\sigma_1 - \sigma_3| - |\sigma_1 + \sigma_3| \sin \phi}{2 \cos \phi}. \quad (10)$$

Equation (10) shows that  $C_{\text{min}}$  increases linearly with  $\tau_{\text{max}}$ . We follow Miller and Dunne (1996) and use  $C_{\text{min}}$  as a proxy for shear failure potential.

The types of fractures that are predicted to form depend on the stress state. Shear fractures form at oblique angles with respect to the principal stresses, whereas opening mode fractures develop perpendicular to the most tensile (least compressive) stress  $\sigma_3$  (Jaeger et al., 2007).

## 2.5 Influence of Topographic Aspect Ratio: Synthetic Calculations

The BEM method can be used to calculate stresses under any topographic profile, not only idealized profiles that are amenable to analytical solutions, like the coordinate mapping of Savage et al. (1985). To illustrate how topography affects the stress distribution in a simple scenario, we used the BEM to calculate topographic stresses for a series of sinusoidal topographic profiles with a common wavelength of 1000 m but different topographic amplitudes (10 to 100m) and lateral tectonic stresses. Our boundary conditions were  $\sigma_{xx} = \text{tectonic stress} + [\nu/(1-\nu)] \rho g y$  and  $\sigma_{yy} = \rho g y$ , with  $\rho = 2650 \text{ kg/m}^3$  and  $\nu = 1/3$ . Each sinusoidal topography was made of a series of 3-4 troughs/peaks and had tapered ends (not shown in Figure 5).

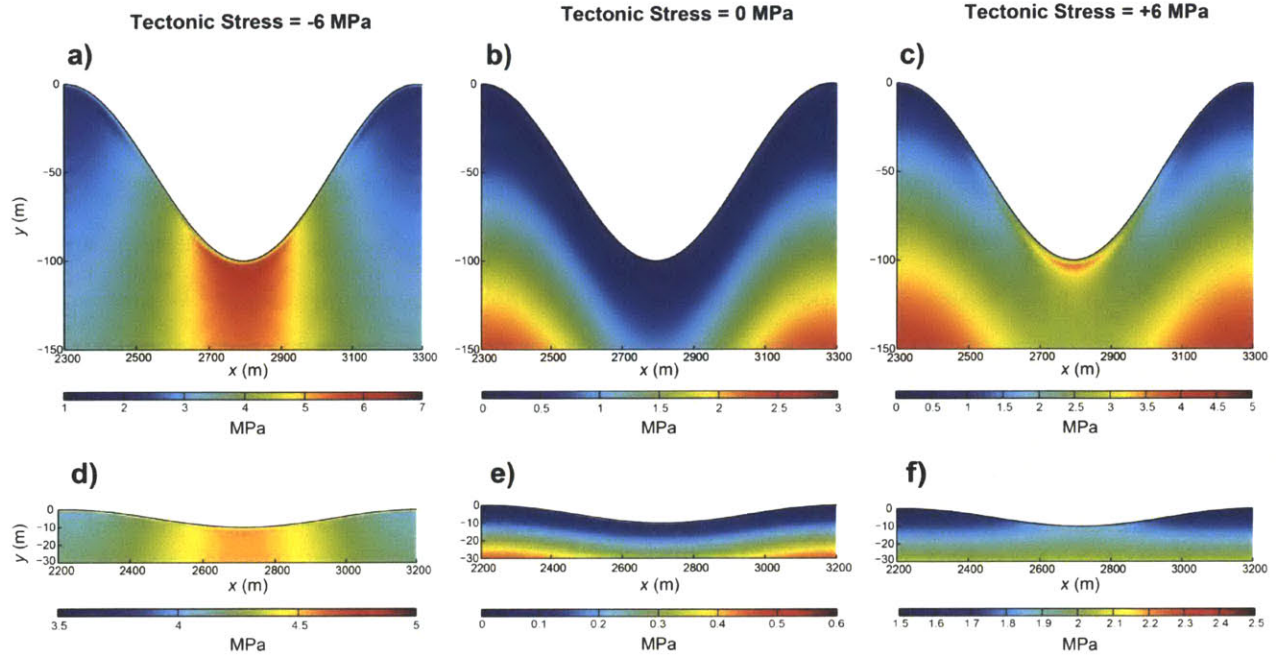


Figure 5:  $C_{\min}$  obtained from the BEM under idealized sinusoidal topography with the same wavelength but different amplitudes and tectonic stresses. Three tectonic stress regimes are shown: compressive (-6 MPa; a,d), tensional (6MPa; c,f) and no tectonic stress (b,e). Poisson's ratio,  $\nu = 1/3$ . The topography, which is vertically exaggerated in each plot, has an amplitude of 50 meters in the upper row and 5 meters in the lower row. The calculation was performed on a profile several wavelengths long to minimize effects of the lateral boundaries; only the middle valley is shown here.

Figure 5 shows plots of  $C_{\min}$  beneath these profiles, calculated with  $\phi = 24^\circ$ . The most obvious difference is that  $C_{\min}$  is larger when tectonic stresses are introduced. It is also clear from Figure 5 that the sign of the tectonic stress and the amplitude of the topography modulate spatial trends in  $C_{\min}$ . With no tectonic stresses (Figure 5b,e),  $C_{\min}$  increases with depth and its change mimics the topographic relief.

Under compressive tectonic stress,  $C_{\min}$  decreases with depth (Figure 5a,d) beneath the valley whereas under tensile tectonic stress, the amplitude of topography determines how  $C_{\min}$  changes with depth beneath the valley;  $C_{\min}$  decreases with depth with high topographic relief (Figure 5c) and increases with depth under low topographic relief (Figure 5f). Beneath ridgetops,  $C_{\min}$  is smaller than beneath the valley and always increases with depth.

This synthetic calculation illustrates three general trends: first, there is a greater susceptibility to shear fracturing under valley floors; second, ridgetops are generally more stable with respect to shear fracturing in the absence of tectonic stresses; and third, the depth gradient of  $C_{\min}$  under ridgetops when tectonic stresses are applied is relief-dependent. Also, if the horizontal tectonic stress is zero (middle column), then topography has a great effect, and the magnitude of  $C_{\min}$  scales in proportion to the topographic relief (Figure 5b,e). When regional tectonic stresses are applied,  $C_{\min}$  is still sensitive to topographic relief, but is controlled primarily by the magnitude of the tectonic stresses (Figure 5a,c,d,f). In short, high regional tectonic stress can mask the effect of topography on local stresses.

# CHAPTER 3

## Application to the Shale Hills, Pennsylvania

### 3.1 Site Description

The Susquehanna/Shale Hills Critical Zone Observatory (SSHO) is a 0.08 km<sup>2</sup> catchment located in the uplands of the Valley and Ridge physiographic province of central Pennsylvania (Figure 6). It was established to investigate the creation, evolution and function of the regolith in the catchment area; the observatory is used to study the groundwater flow, date groundwater, estimate soil-weathering rates, and measure the residence time of solutes in the subsurface (Singha et al., 2012; unpublished manuscript). It contains a stream (a tributary of Shavers Creek) that flows west between narrow ridges. The average local relief (valley floor to ridgetop) is 20 m and the average channel gradient upstream is 4.5% (Lynch, 1976, in Jin et al., 2010). The catchment is eroded into the Silurian Rose Hill Formation of the Clinton Group (Jin et al., 2010), which consists of shale with a few interbedded limestones of variable thickness (Lynch, 1976 in Jin et al., 2010). Locally, the Rose Hill Formation is a fractured fossiliferous shale layer with interbedded limestone and fine-grained sandstone (Singha et al., 2012; unpublished manuscript). Although the area is currently tectonically inactive, the geologic structure in the region is characterized by tight, plunging folds in Silurian-aged strata. Average strike and dip measurements from exposures of bedrock in the catchment floor are S54°W and 76°NW, respectively (Jin et al, 2010). Steeply dipping beds are seen in the center of the catchment area suggesting folds of different scales superimposed on the dipping beds (Singha et al., 2012; unpublished manuscript). Much shallower bedding dips of approximately 30° are observed in borehole image logs (Kuntz et al., 2011) and in outcrops near the wells at the mouth of the valley (Tim White, personal communication).

Pennsylvania is part of the eastern North American stress province which is a compressive stress regime. The stress is thought to be associated with tectonic plate boundaries, with two

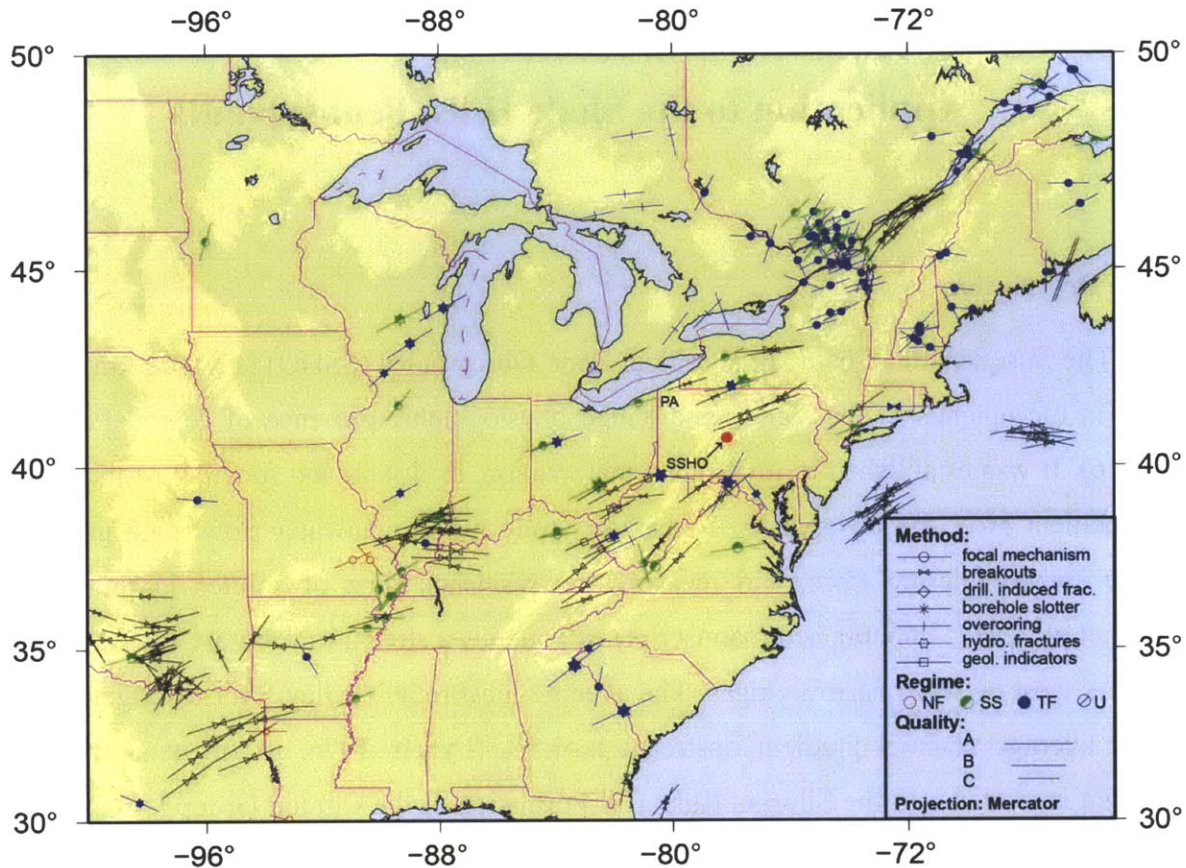


Figure 6: The stress map of central and eastern North America showing the directions of maximum horizontal stress ( $S_{Hmax}$ ). SSHO (Longitude: 40°39'N; Latitude: 77°54'W) is indicated with a red circle in Pennsylvania (PA). The different symbols represent different methods used to measure  $S_{Hmax}$  in different faulting regimes: NF = normal faulting, TF = thrust faulting, SS = strike slip, U = unknown regime. A, B, and C represent the data ranking quality outlined in Zoback and Zoback (1989) with A being the highest quality data. The map was prepared using CASMO, a web-based service for accessing the World Stress Map database (Heidbach et al., 2008; [http://dc-app3-14.gfz-potsdam.de/pub/introduction/introduction\\_frame.html](http://dc-app3-14.gfz-potsdam.de/pub/introduction/introduction_frame.html); accessed in September, 2012).

models proposed for the source of compression: ridge push and basal drag (Zoback and Zoback, 1989). Seismic activity increasing from west to east within the craton and the extensional stress regime in the southern Great Plains stress province are indications favoring the ridge push model over the basal drag model (Zoback and Zoback, 1989). Plumb and Cox (1987) report trends in the northeastern United States of the most compressive horizontal stress ( $S_{Hmax}$ ) of  $N54^{\circ}E \pm 7^{\circ}$ , and

Zoback and Zoback (1980, 1989) report  $S_{Hmax}$  trends of NE to ENE in the central and eastern stress provinces. Zoback and Zoback (1989) describe the Midcontinent stress province as having a poorly defined eastern boundary that crosses the Valley and Ridge province, which includes the SSHO, in the north. Under either of these conditions, many of the fractures beneath the valley would be susceptible to slip, regardless of how they originated. Thus, even if topographic stresses did not trigger the formation of all fractures in the bedrock, they could still cause re-fracturing and sliding on older fracture planes, and could therefore have a strong influence on the abundance of active, open fractures.

The SSHO site has two key advantages for our study. First, the site's topography has been surveyed with high-resolution airborne laser altimetry through the State of Pennsylvania's PAMAP program (<ftp://pamap.pasda.psu.edu>) and by the National Center for Airborne Laser Mapping (NCALM). Second, optical image logs from boreholes located in the valley permit detailed observations of fractures.

### **3.2 Topography and Stress Calculations**

I used laser altimetry data to extract a topographic profile perpendicular to the valley axis (N22°E) along a transect that passes through CZMW 1 and is within a few meters of the other three boreholes (Figure 7). The valley profile (Figure 7b) is asymmetric, and therefore the stresses cannot be modeled well using the analytical solution of Savage et al. (1985). Given the elongated shape and relatively gentle longitudinal profile of the valley, we assume that a two-dimensional treatment of the state of stress is reasonable. The measured transect and the added tapered sections (Figure 7a) are 4284 m long horizontally so that the valley and ridges of interest are far from the tips of the crack representing the ground surface. A mesh of subsurface observation points where stresses will be calculated is chosen, with the  $x$  locations generally beneath element midpoints (which results in improved accuracy; Figure 3) and  $y$  locations at regular depth increments,  $\Delta y = 0.5$  m. The uppermost observation points are chosen to be 0.05 m from the surface. To reduce the

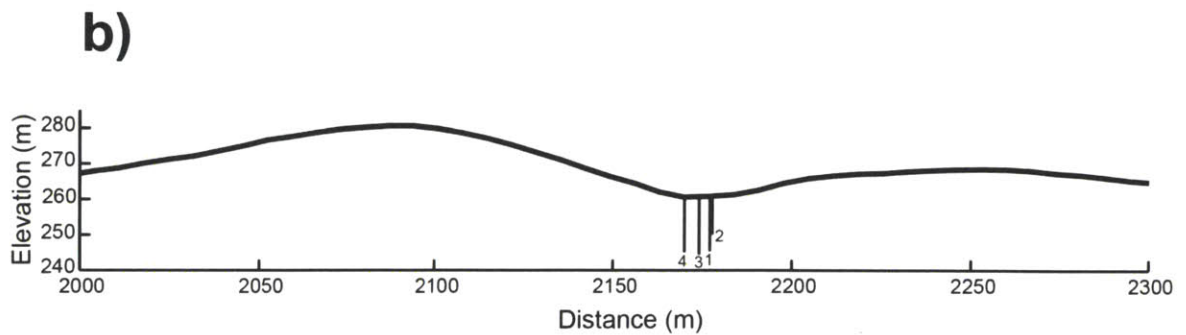
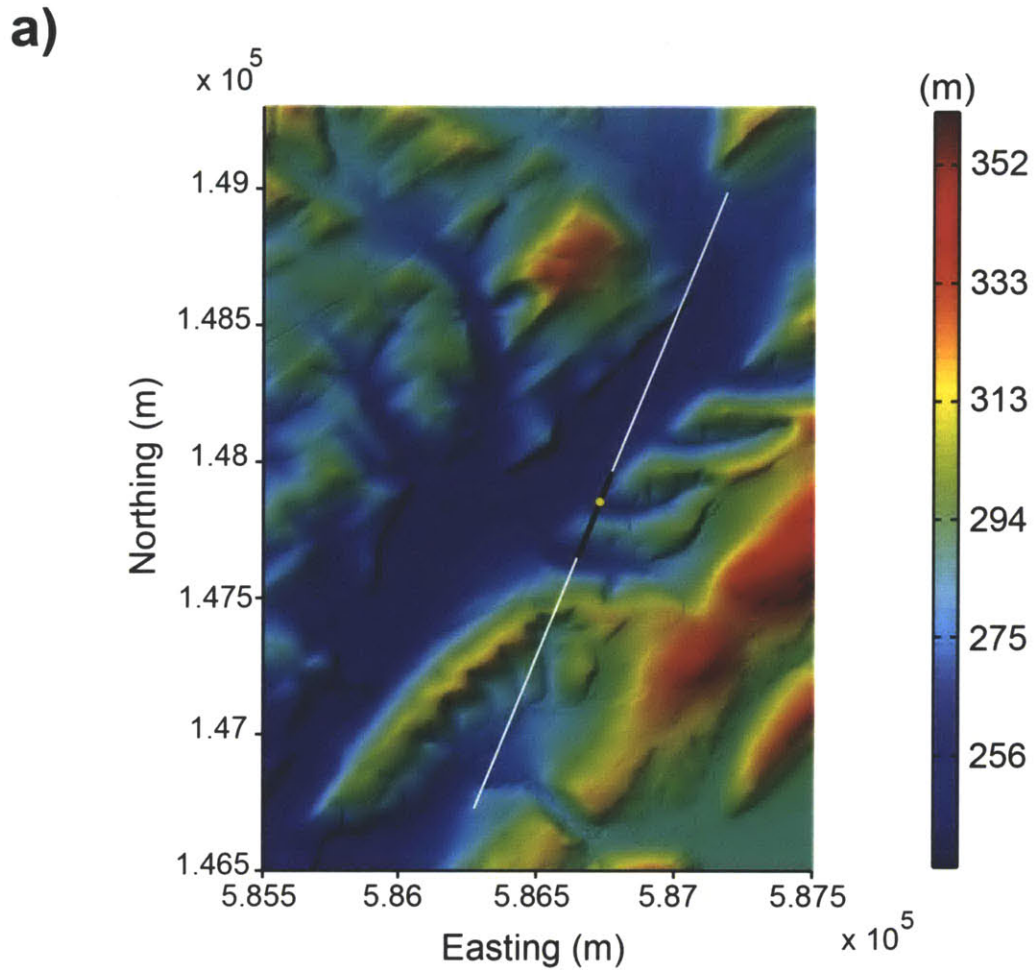


Figure 7: (a) A shaded relief map of the Shale Hills study site and surroundings showing well locations (yellow circles) and the trace of the cross-section used in this study (white line). (b) Topographic profile along the black transect in (a) showing locations and depths of wells. The transect passes through well CZMW 1, and wells CZMW 2, 3, and 4 are projected onto the cross-section. All wells are within 3m of CZMW 1.



total number of elements for reasons of computational efficiency, we use fine elements ( $\Delta x = 7$  m; defined and dictated by the resolution of topographic maps available for the region) under the topography of interest and part of the tapered sections ( $911 \text{ m} < x < 3463\text{m}$ ), and coarse elements ( $\Delta x = 16$  m) for the extended tapered sections (for  $x < 911$  m and  $x > 3463$  m).

We are aware of only a few estimates of tectonic stresses in the region (Heidbach et al., 2008. Figure 6). The compilation of stress measurements in Heidbach et al. (2008) is believed to be for measurements taken at depths greater than 100 m as it contains data reported from breakout analysis, focal mechanisms, hydraulic fracturing, etc. Zoback (2007) states that in situ stress measurements at shallow depth cannot be used for tectonic stress compilations; tectonic stresses at shallow depths are very small due to low frictional and tensile strengths of near-surface rocks. Therefore, the tectonic stress magnitude reported on the World Stress Map Project site (<http://dc-app3-14.gfz-potsdam.de/index.html>) may not be suitable to use to calculate the stress distribution in the shallow subsurface at SSHO. Miller and Dunne (1996) report tectonic stresses in the northeastern United States of  $-6.9 + 0.035y$  MPa for the maximum horizontal stress ( $S_{Hmax}$ ) and  $-6.0 + 0.017y$  MPa for the minimum horizontal stress ( $S_{Hmin}$ ) (where  $y$  is depth, and both  $y$  and compressive stresses are negative). Given the small difference between the reported values of  $S_{Hmax}$  and  $S_{Hmin}$  (Miller and Dunne, 1996), I used the BEM to calculate stresses beneath the SSHO topographic profile (Figure 7) assuming the tectonic stress to have the magnitude of the lowest reported surface horizontal compressive stress (-6 MPa) in order not to mask the effect of topography at SSHO.

The boundary conditions are  $\sigma_{xx} = \text{tectonic stress} + [\nu / (1 - \nu)] \rho g y$  and  $\sigma_{yy} = \rho g y$ , with  $\rho = 2650 \text{ kg/m}^3$  and  $\nu = 1/3$ . Horizontal stresses ( $\sigma_{xx}$ ) are compressive throughout the landscape, but are smallest under the ridgetops (~2-5 MPa) and largest under the valley floor (~9-10 MPa) (Figure 8a). Vertical stresses ( $\sigma_{yy}$ ) are also compressive (Figure 8b). The maximum shear stress (Figure 8c) decreases sharply with depth beneath the valley and increases with depth beneath the ridges. The cohesion at shear failure,  $C_{min}$  (Figure 8d), has a pattern similar to the maximum shear stress, with remarkably different trends in  $C_{min}$  under the valley floor and under ridgetops. The zone most susceptible to topographically induced shear fracturing is a shallow zone beneath the

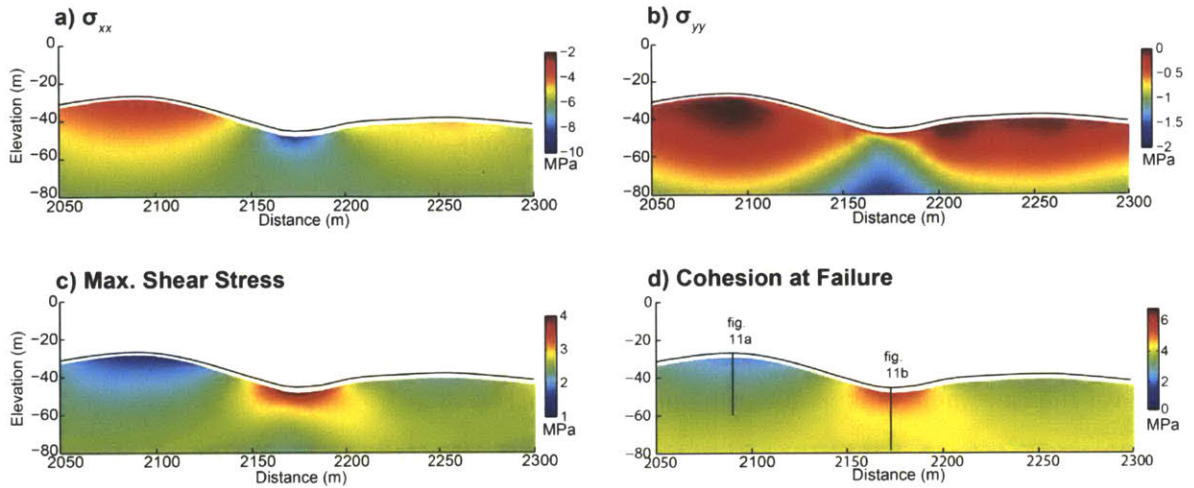


Figure 8: Plots of (a)  $\sigma_{xx}$ , (b)  $\sigma_{yy}$ , and (c)  $\tau_{max}$  as obtained from the BEM for the topographic profile in Figure 7, with a 6 MPa compressive tectonic stress,  $\rho = 2650 \text{ kg/m}^3$ , and  $\nu=1/3$ . (d) Cohesion at failure,  $C_{min}$ , calculated with  $\phi = 24^\circ$ . The locations of the depth profiles in Figures 11a and 11b are indicated.

valley floor. Zones near the surface beneath tall ridges or deep below the valley are more resistant to fracturing, with little to no cohesion required to prevent failure.

### 3.3 Borehole Structural Analysis

Data on the locations and orientations of subsurface fractures from borehole logs constitute the key information we use to test our model predictions. Image logs (e.g., Figure 9. Appendix B) from the four boreholes in the valley bottom shown in Figure 6 were acquired with an Optical Borehole Imaging (OBI) tool manufactured by Mount Sopris Instruments. The OBI is an optical televiewer that produces a continuous,  $360^\circ$ , oriented image of the borehole wall using a downhole charge-coupled device (CCD) camera. The tool has a 3-axis magnetometer and two accelerometers that allow for precision in calculating borehole deviation from vertical and orientation of the image. Image resolution of the logs was roughly 0.5 mm vertically and 0.33 mm azimuthally. The image logs were processed with WellCAD, a PC-based well log processing package. They were oriented to magnetic north. No deviation or casing-effect corrections were

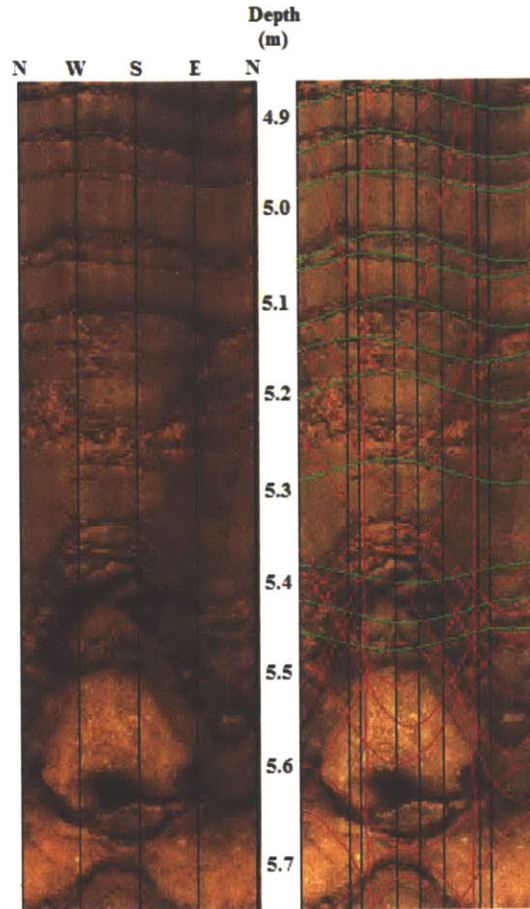


Figure 9: A section of an OBI log taken from CZMW 4. The left image shows untraced bedding and fracture planes. The right image log shows the same section of the borehole wall with structural features traced. Green low-amplitude traces indicate gently dipping bedding planes, and red high-amplitude traces indicate steeply dipping fracture planes. Image orientations are relative to magnetic north.

made, as the wells are vertical and cased with polyvinyl chloride (PVC) pipes. Fractures could not be mapped within 3 meters of the ground surface, because boreholes were cased to 3 m depth.

The main structures observable in the borehole image logs are natural fractures and bedding planes. These planar features have sinusoidal traces on the flattened image logs (Figure 9). The phase angle of a trace relative to a reference mark (North) yields the strike of the planes, and the trace amplitude yields the dip (Luthi, 2001; Serra, 1989). Each fracture and bedding plane was traced eight times, and the strike and dip of a feature were assigned based on the arithmetic

averages of the eight strike directions and eight dip magnitudes. A scatter in the repetitive picks and the misfit of the average trace with a planar feature reflect a low certainty tracing the planar feature. Features with incomplete sine waves were the hardest to trace. Neither drilling-induced fractures nor borehole breakouts are well developed in the boreholes. No clear displacement was seen along structural features. A few traces suspected to be healed or partially healed fractures are visible in the thick shale layer in well 1. Because of the image quality, image acquisition technique (camera vs. resistivity mapping), and their scarce occurrence, healed fractures were not grouped into a separate fracture set nor used to interpret old stress regime(s) in the area. I do not believe that the few healed fractures add to the scatter in the fracture orientations. The observation that they are still healed suggests that they are either older than other fractures or too deep for the topography to influence and initiate their reactivation.

The bedding planes were traced where weathering or differential erosion highlighted surfaces separating laminations or beds. Bed traces on the image logs were continuous; the complete sine waves suggest depositional features rather than structural ones and their consistently low amplitudes reflect gentle dip angles. Many fractures, on the other hand, had generally incomplete sine waves where only the troughs or portions of its sides are seen. Steeply-dipping en-echelon traces, although rarely seen, may be poorly-developed drilling-induced fractures. The strike direction of drilling-induced fractures indicates the direction of  $S_{Hmax}$ . The poor development and rare occurrence of the drilling-induced fractures indicates a low tectonic stress magnitude. The absence of breakouts indicates far-field horizontal stresses ( $S_{Hmax}$  and  $S_{Hmin}$ ) with comparable and similar magnitudes. This is consistent with the regional tectonic stresses reported in Miller and Dunne (1996). In highly deformed and fractured zones, some fractures have complete traces/sine waves and occur in steep conjugate sets. This latter family of fractures might be younger than the one with partial sine waves (partial sine waves indicates erosion of an already fractured bed/formation).

Figure 10 shows the poles to fracture and bedding planes in the subsurface. These data show clustering in the orientations of both fractures and bedding. The fractures beneath the valley generally dip steeply to the SE or NW. The bedding beneath the valley generally dips to

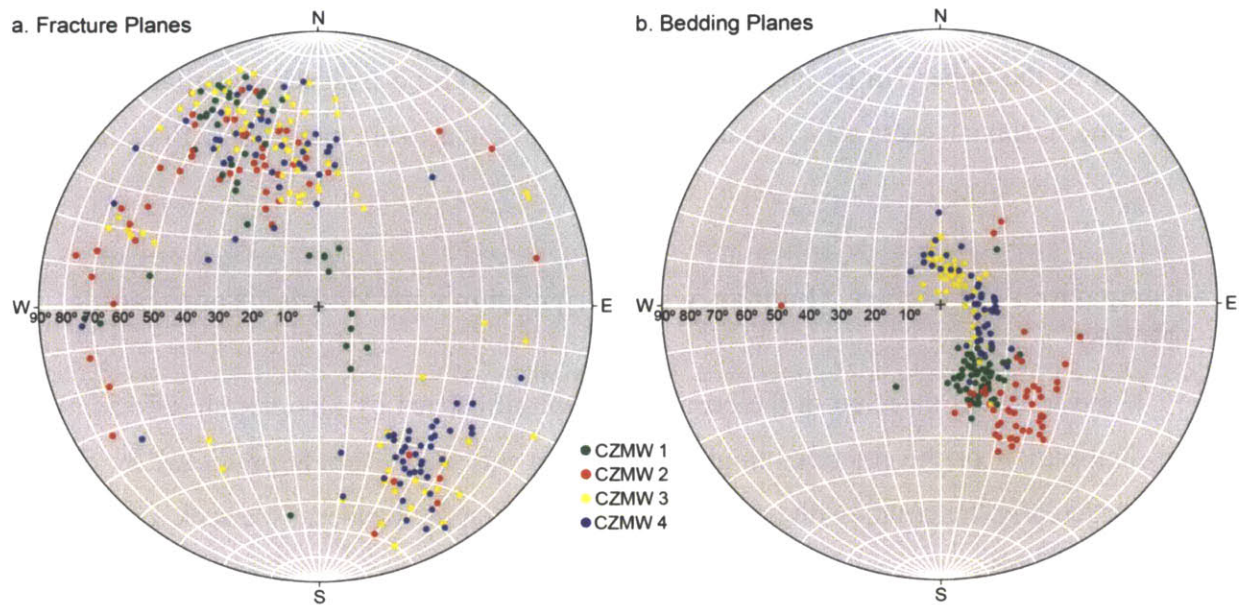


Figure 10: Stereonets showing arithmetic averages (see text) of the (a) fracture and (b) bedding plane orientations in the wells. The plots are Schmidt plots showing the intersections of the poles to the planes with the lower hemisphere. Gentle-dipping planes plot near the center of the stereonet whereas steeply-dipping planes plot near the primitive circle. Dip angle magnitudes are indicated on the stereonet.

the NW. A few bedding planes in CZMW 3 and CZMW 4 dip to the S and W. The gentle bedding dips contrast with Jin et al. (2010) and agree with observations of outcrops (Tim White, personal communication; Kuntz et al., 2011). The data also reveal scatter in wells CZMW 2, CZMW 3 and CZMW 4 (fractures striking WSW-NW) partly due to incomplete fracture traces, which increased the uncertainty in the sine wave fit; the presence of what appear to be healed fractures (traces with bright colors suggesting cement-filled fractures/joints) in some deeper shale sections; and highly fractured/faulted and perturbed middle sections in some of the wells where many fractures intersect and individual fracture traces are less clear. Most of the subsurface fractures are roughly perpendicular to bedding. Some of the fractures, however, are at shallow angles with respect to bedding, especially in borehole CZMW 3. The variation in the absolute orientations of the fractures and the variation in the orientations of the fractures with respect to bedding suggest that subsurface fractures reflect multiple episodes of deformation. The prediction of Miller and Dunne

(1996) and Augustinus (1995) of tensile fractures forming right beneath the valley floor could not be checked as the upper 3m of each borehole are cased with no image log available. At greater depth (>3m), a triaxial stress state dominates, and shear fractures are more likely to develop.

### **3.4 Comparison of Fracture Abundance and Orientation with Modeled Topographic Stresses**

If the fractures detected in the boreholes were influenced by topographic effects, then the spatial distribution of the fractures might well mirror the spatial trends predicted by our stress model, particularly the trends with depth below the topographic surface. We seek a proxy for the intensity of fracturing that will be relevant to near-surface hydrologic and geomorphic processes that we can compare with our model predictions of  $C_{min}$ . One simple proxy is the number of fractures per unit vertical depth within each borehole, which we refer to as the fracture abundance.

The strongest vertical trends in  $C_{min}$  are beneath ridgetops and the valley floor (Figure 8d). Under the ridgetop,  $C_{min}$  increases with depth, whereas  $C_{min}$  declines with depth under the valley floor. Calculations of  $C_{min}$  for various angles of internal friction,  $\phi$ , show that the shapes of these trends are largely independent of  $\phi$  (Figure 11 a,b). The main effect of  $\phi$  is to scale the magnitude of  $C_{min}$ . No logged boreholes exist on the ridgetops, ruling out a comparison of ridgetop fracture abundance with  $C_{min}$  beneath the ridges. Boreholes do penetrate the valley floor, though, so I focus my attention there. The rate at which our modeled values of  $C_{min}$  decrease with depth under the valley floor is steep in the uppermost 10 m of the wells and gentler at greater depths (Figure 11). Figure 11 compares these trends in  $C_{min}$  with the fracture abundance measured in the four boreholes near the valley axis at the SSHO. The measured fracture abundance declines from an average of roughly 10-15 fractures/m at a depth of 5 m to less than 5 fractures/m at a depth of 15 m (Figure 11c). This reduction in fracture abundance with depth is similar to the predicted decline in  $C_{min}$  with depth beneath the valley floor (Figure 11b).

Working in the upper 15 m of the subsurface and having  $S_{Hmax}$  and  $S_{Hmin}$  with comparable

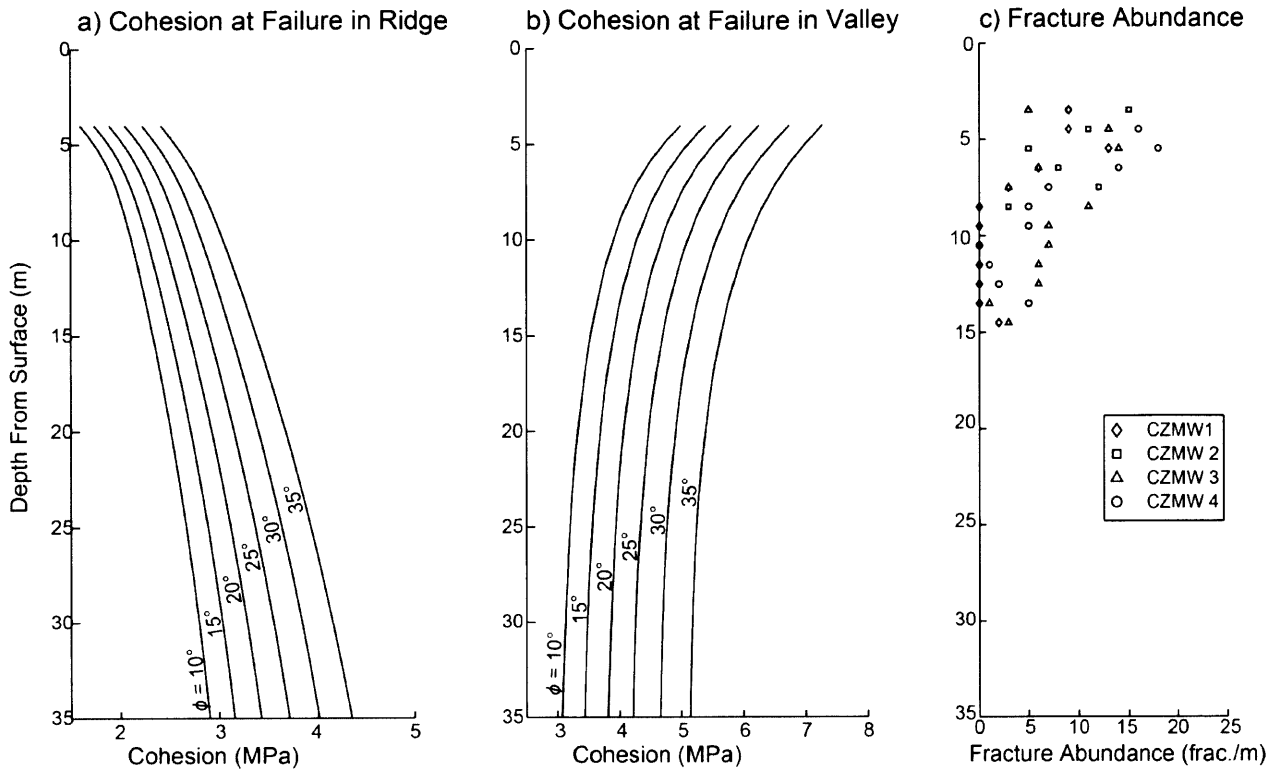


Figure 11: Depth profiles of cohesion-at-failure,  $C_{min}$ , under (a) the ridgetop and (b) the valley floor at the locations shown in Figure 8d. Curves are shown for internal friction angles ( $\phi$ ) ranging from  $10^\circ$  to  $35^\circ$ . (c) Plot of fracture abundance in borehole image logs as a function of depth. Fracture abundance could not be measured within 3 m of the surface because boreholes are cased to 3 m depth.

magnitudes (Miller and Dunne, 1996), I assume that the overburden is the least principal stress. The BEM code used allows the calculation of the principal stress orientation (Figure 12a); in the shallow subsurface, the most compressive stress,  $\sigma_1$ , is parallel to topography. In deeper sections,  $\sigma_1$  becomes horizontal, and therefore parallel to the tectonic stress applied in the model. The depth at which the maximum principal stress becomes aligned with tectonic stress provides an estimate of the depth below which the effect of topography is no longer significant. This depth is roughly 15-20 m below surface.

The topographic transect is taken along  $N22^\circ E$ , perpendicular to the valley direction in order to have the maximum topographic relief to work. The transect is at  $20-40^\circ$  to the reported

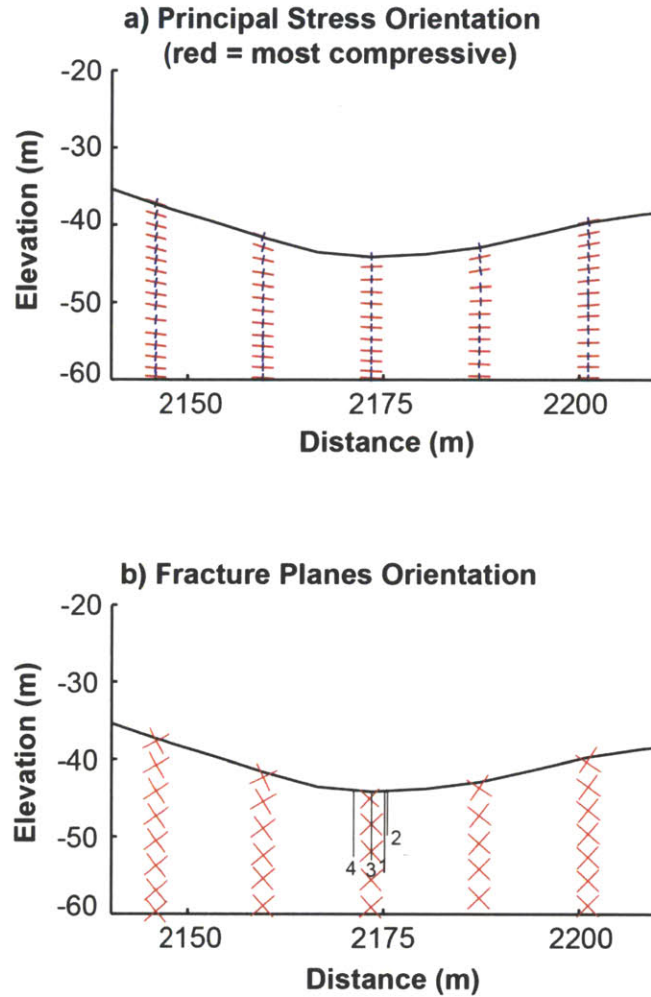


Figure 12: Orientations of (a) principal stresses obtained from the BEM and (b) predicted fracture planes under the valley.

$S_{Hmax}$  direction at SSHO. The BEM calculates the orientations of the principal stresses (Figure 12a), and I infer the orientation of potential conjugate sets of fracture planes where the maximum shear stress is expected. The planes with maximum shear stress form at  $\pm 45^\circ$  from  $\sigma_1$  (Figure 12b). Potential fracture planes, thus, strike N70°W and N20°E.

Following Anderson's theory of faulting, potential strike directions for faulting planes can range between being parallel to  $S_{Hmax}$  (mode I fractures and Normal faulting regime), forming  $30^\circ$  with  $S_{Hmax}$  (strike slip regime), or normal to  $S_{Hmax}$  (thrust faulting regime). The structural data



from the boreholes at SSHO (Figure 10) show that we have multiple generations of fractures. The dominant faulting regime is strike slip as many of the well fractures having strike directions 20-45° from  $S_{Hmax}$ . Few fractures have their strike direction parallel to  $S_{Hmax}$ ; these might be the youngest generation mode I fractures.

# CHAPTER 4

## Discussion, Conclusions, and Implications

### 4.1 Discussion

The model presented is a useful tool for studying the effects of topographic stresses and predicting areas of high failure potential and relative fracture abundance. The main advantage over previous models of topographic stress is that the BEM does not require the topography to conform to an idealized, symmetric shape that can be described with a simple analytical function. Another advantage is that it can calculate stresses beneath a topographic profile that includes multiple landforms, rather than a single valley or ridge. As in the existing analytical models, however, the limitation of our stress calculations to plane strain conditions means that the effects of two-dimensional topography on the three-dimensional stress distribution are not considered. As the main objective of this work is study the effect of topography on the stress distribution, a topographic transect along the valley floor gives stresses beneath a sloping surface with no significant topographic relief, and developing a 3D model that incorporates multiple transects is beyond the scope of this work.

Drilling boreholes on a ridgetop deeper in the valley was attempted, but taking the drilling rig up the ridge and stabilizing it for drilling was not successful. I acknowledge the importance of drilling more boreholes, as observations would permit a more complete test of the predicted effects of topographic stress. In particular, structural data from a ridgetop borehole would provide a test of whether a more uniform fracture abundance with depth, or perhaps even an increase in fracture abundance with depth, is observed beneath ridges, consistent with the trend in  $C_{\min}$  in Figure 11a.

Another way to test the influence of topography would be to compare the measurements presented here with measurements from boreholes in a site with comparable regional tectonic stress but higher topographic relief. If such a site displayed comparable trends in fracture

abundance over a deeper depth than in the SSHO, it would support the prediction of Savage et al. (1985), McTigue and Mei (1996), and Clarke and Burbank (2011) illustrated here in Figure 8, that the effects of topographic stress should scale with topographic relief.

Observations in the wells and BEM predictions are consistent in supporting the hypothesis that both the ambient stresses, which reflect the tectonic context (Martel, 2000), and topography affected the fracture abundance. The observed decrease of fracture abundance with depth (Figure 11c) beneath the valley floor in all four wells is consistent with my predictions, as the cohesion required to prevent fractures decreases with depth (Figure 11b). This occurs for the study area because the maximum shear stress decreases with depth more rapidly than the mean compressive stress increases with depth (see Equation 9). The rate that these variables change in general would depend on the ambient stress field and the topography. Our comparison of predicted topographic stresses with observed fractures beneath the valley floor is consistent with the hypothesis that topographic stresses influence the formation or reactivation of rock fractures in the shallow subsurface; the stresses due to the valley's cross-sectional shape and 20-30 m relief might indeed have contributed to the fracture patterns observed in the uppermost 15 m of the subsurface at the SSHO, where topography is predicted to have its greatest influence (Figure 7). The principal stress orientations stop being parallel to the topography 20 m from the surface; the maximum principal stress around that depth becomes horizontal (parallel to the applied tectonic stress) and the overburden becomes vertical, indicating that the effect of the topographic relief decreases with depth.

Although the image log of CZMW 1 in Appendix B shows a thick shale layer that extends from 7-15 m with no open fractures seen in it, the predicted decrease in fracture abundance with depth does not mean that no fractures will be seen below 10-15m. A more linear trend between depth and  $C_{\min}$  is calculated deeper in the boreholes, where topographic effects are less significant (Figure 11a,b), suggesting that the decline in fracture abundance with depth will be more gradual. This is consistent with Clarke and Burbank's (2011) conclusions that linear P-wave velocity gradient in the shallow multilayered subsurface is caused by non-linear decline in fracture density and is independent of rock types. Clarke and Burbank (2011) argue that tectonic

fracturing produced a uniform/linear velocity and that the geomorphic processes focused within the near surface (0-15m) produce the depth-dependent or nonlinear fracture density change. Their fracture density profile is very similar to the decline in fracture abundance in Figure 11c; topographic stress is a possible mechanism that can explain Clarke and Burbank's (2011) fracture abundance in the shallow subsurface.

The fracture orientations obtained in the wellbore agree with the structural history of the location and the (recent) horizontal stress directions reported (Zoback and Zoback, 1980 and 1989; Plumb and Cox, 1987; Heidbach et al., 2008). The scatter in the borehole fracture orientations reflects multiple generations of fracturing events and spatial variability in rock properties and structure within the site. The medium, as seen from image logs, is not homogeneous (shale and carbonaceous layers) nor isotropic (heavily fractured sections, laminations and bedding planes) as assumed by the BEM; anisotropy and variations in lithologies, porosities, pore pressure, and cementation are not taken into consideration by the model. Stress distribution and concentrations at pore cavities and effective stress variations due to pore pressure affect the stress distribution in the subsurface and, consequently, the fracture orientation predictions. Without a careful study of how the topography evolved with time and a more thorough understanding of the tectonic history in the region, it is difficult to separate the fractures into various generations and point out which one was most influenced/caused by the present-day topography. Pre-existing fractures due to the tectonic history could have been reactivated; a process that can release strain energy gradually and more efficiently than forming new fractures. Reactivated old fractures might be the ones most clearly seen in the wells. It is therefore understandable that the stress model does not correctly predict the orientations of all observed fractures.

## **4.2 Summary and Conclusions**

We used a two-dimensional numerical boundary element method (BEM) to calculate elastic subsurface stresses induced by an arbitrary topographic profile. The BEM solutions for

symmetric valleys and ridges match previously published analytical solutions well. Unlike the analytical solutions, the BEM is not limited to topography that can be described by simple functions, and it can calculate stresses for transects through multiple landforms rather than single ridges or valleys. The sign and magnitude of tectonic stresses can easily be included in model calculations. In sites where topographic stresses influence rock fracture, the model presented here provides a framework for studying the effects of topography on subsurface hydrology, as well as possible feedbacks between rock fracture and landform evolution.

We used the BEM to calculate stresses beneath a topographic cross section through the Shale Hills Critical Zone Observatory in Pennsylvania. The model predicts different stress conditions beneath the valley floor and adjacent ridgetops. With a compressive regional tectonic stress of -6 MPa, the predicted horizontal stress is compressive throughout the landscape, is largest (~9-10 MPa) in the valley, and is smallest (~2-5 MPa) under the ridgetops. Vertical stresses under the valley floor and the ridgetops are also compressive, but generally are less than the horizontal compressive stress by a factor of 5-10. From the stress calculations, we derived the minimum cohesion needed to prevent shear failure,  $C_{\min}$ , as a proxy for the susceptibility of the rock to the formation or reactivation of shear fractures. The trends of  $C_{\min}$  with depth differ between the valley and ridges, with  $C_{\min}$  increasing with depth under the ridgetops and decreasing with depth under the valley floor. This predicted decline in  $C_{\min}$  under the valley floor compares well with a measured decline in fracture abundance in four boreholes near the valley axis at the Shale Hills site, consistent with the hypothesis that topographic stresses influence the formation or reactivation of fractures. Future logging of a ridgetop borehole would provide a more complete comparison of the observed fracture patterns with the predicted topographic stresses. Comparing the predicted fracture orientations to fracture planes traced on the image logs, it is clear that the BEM poorly predicts fracture orientations as it assumes a homogeneous and isotropic subsurface with no means to incorporate the structural history and multiple fracturing events.

### **4.3 Implications and Recommendations for Future Work**

The ability to calculate topographic stresses and predict fracture patterns beneath any topographic profile provides a means of exploring the effects of topographically induced fracturing on other landscape processes. Predicted spatial trends in fracture abundance and orientation could allow hydrogeologists to map spatial variations in permeability, and thereby study the effects of surface topography on subsurface flow and transport (Singha et al., unpublished transcript). Civil engineers could use predicted topographic stresses to help calibrate their models of subsurface density, porosity, and velocity. The effects of subsurface fractures on bulk rock strength, rock surface area, and groundwater flow could also influence rates of rock weathering, soil production, bedrock erosion, and rock wall recession (Moore et al., 2009). Predicted fracture abundance could potentially be used as a proxy for the rates of these processes in long-term landscape evolution models (Moore et al., 2009; Dühnforth et al., 2010). Feedbacks between landform evolution and rock fracture (Moore et al., 2009) might include the previously proposed positive feedback between valley incision and stress concentration at the valley axis (Molnar, 2004), as well as effects introduced by the depth dependence of topographic stress. For instance, topographically induced fractures beneath valley floors may be limited to the shallow subsurface, creating a shallow, highly permeable zone overlying relatively intact and stable rock. This might limit the penetration of shallow groundwater flow and slow weathering within valleys. A more gradual decline in fracture abundance with depth below ridgelines might create a deeper zone of accelerated weathering and enhanced rock erodibility. All these reasons emphasize the need and importance of dynamic models (Augustinus, 1995; Moore et al., 2009) first to incorporate parameters describing the erosive agent (glaciation period and erosion potential) and to describe landform evolution with feedback incorporating rock properties and changes in its strength as it gets fractured and eroded. Dynamic models and feedback incorporating changes in the medium properties and changes in landscape and topography constitute a logical extension of my work and an outline to study landform evolution.

## Appendix A

### Comparison Between Analytical and Numerical Methods

We compared the outputs of the BEM (which is implemented in a code referred to as 2dd) and the analytical solution of Savage et al. (1985) and Savage and Swolfs (1986) (which is implemented in a code referred to as rvt) to check the consistency of the methods. We used both approaches to calculate stresses beneath symmetric profiles of a ridge and a valley produced with the conformal coordinate mapping of Savage et al. (1985), with  $a = 40$  and  $b = 20$  (ridge) and  $a = 16$  and  $b = -8$  (valley). The magnitudes of  $a$  and  $b$  were chosen to produce ridge and valley aspect ratios similar to those at the SSHO. The stress distributions under the symmetric ridge and valley were calculated using a constant tectonic compressive stress of -6 MPa and  $\nu = 1/3$ .

Figure A-1 shows color plots of stresses and  $C_{\min}$  for the ridgeline, and Figure A-2 shows color plots of the stresses and  $C_{\min}$  for the valley. The numerical and analytical solutions match very closely except for a shallow zone immediately beneath the topographic surface. This difference appears to arise from numerical errors in the BEM solution very close to element endpoints. A comparison of depth profiles of  $C_{\min}$  beneath the ridge (Figure A-3a) and valley (Figure A-3b), however, indicates that this discrepancy disappears at depths below the first point near the surface. All of our borehole fracture observations are at depths deeper than 3 m, where all quantities predicted by the two methods agree very closely.

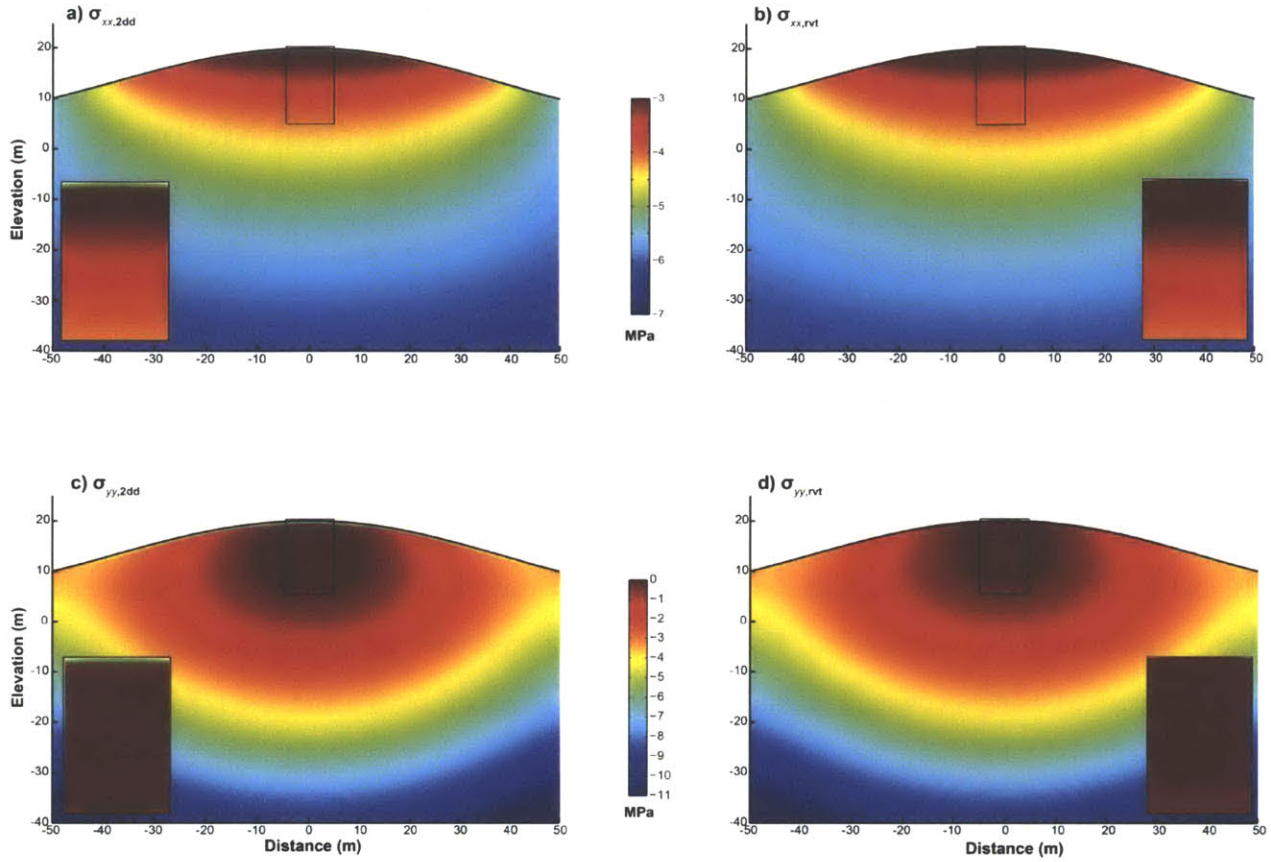


Figure A-1: A comparison of analytical solutions and BEM solutions for a symmetric ridge generated with the conformal coordinate mapping of Savage et al. (1985), with a shape similar to the SSHO ridgelines ( $a = 40$  and  $b = 20$ ). (a)  $\sigma_{xx,2dd}$ , (b)  $\sigma_{xx,rvt}$ , (c)  $\sigma_{yy,2dd}$ , (d)  $\sigma_{yy,rvt}$ , (e)  $\tau_{max,2dd}$ , (f)  $\tau_{max,rvt}$ , (g)  $C_{min,2dd}$ , and (h)  $C_{min,rvt}$  are calculated with a 6 MPa compressive tectonic stress,  $\rho = 2650 \text{ kg/m}^3$ , and  $\nu = 1/3$ . Cohesion at failure,  $C_{min}$ , is calculated with  $\phi = 24^\circ$ . Insets in (a-d) illustrate the deviation of the BEM solution from the analytical solution within approximately 1m of the land surface.



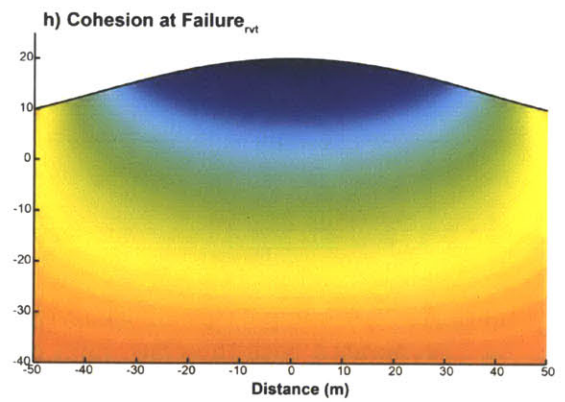
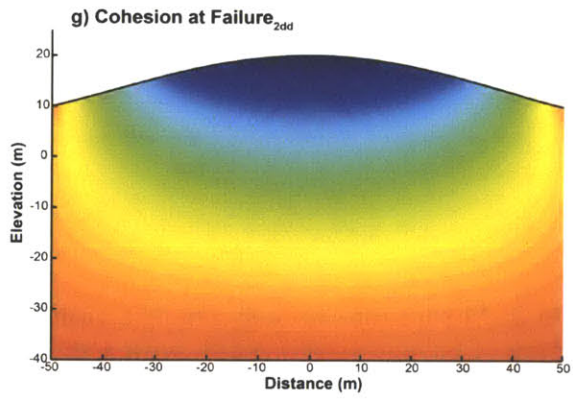
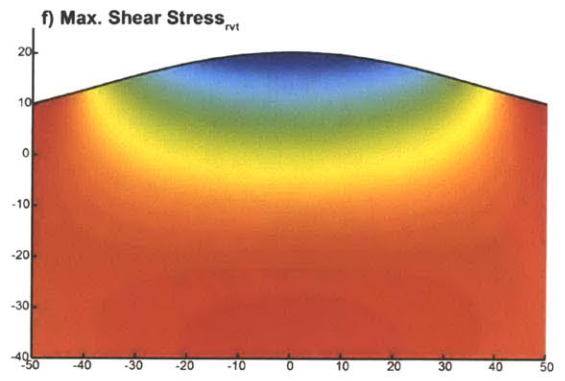
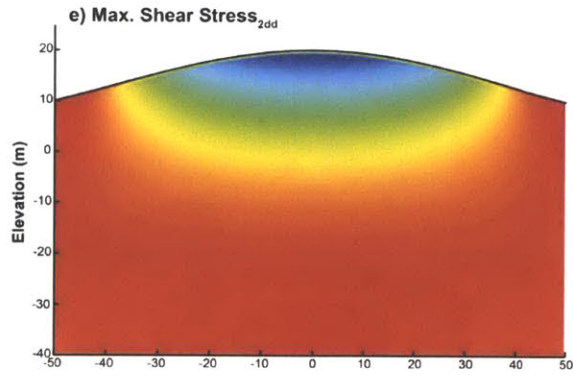


Figure A-1: Continued.

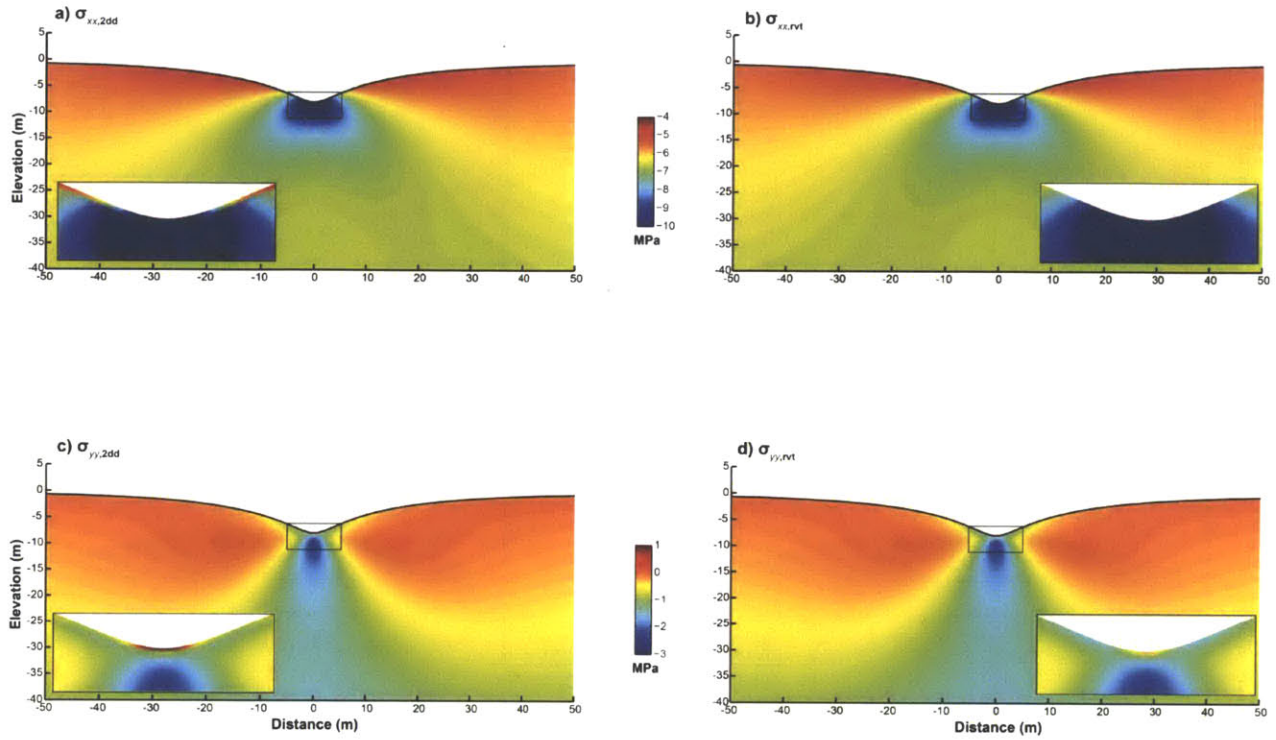


Figure A- 2: A comparison of analytical solutions and BEM solutions for a symmetric valley generated with the conformal coordinate mapping of Savage et al. (1985), with a shape similar to the SSHO valley ( $a = 16$  and  $b = -8$ ). (a)  $\sigma_{xx,2dd}$ , (b)  $\sigma_{xx,rvt}$ , (c)  $\sigma_{yy,2dd}$ , (d)  $\sigma_{yy,rvt}$ , (e)  $\tau_{max,2dd}$ , (f)  $\tau_{max,rvt}$ , (g)  $C_{min,2dd}$ , and (h)  $C_{min,rvt}$  are calculated with a 6 MPa compressive tectonic stress,  $\rho = 2650 \text{ kg/m}^3$ , and  $\nu = 1/3$ . Cohesion at failure,  $C_{min}$ , is calculated with  $\phi = 24^\circ$ . Insets in (a-d) illustrate the deviation of the BEM solution from the analytical solution within approximately 1m of the land surface.

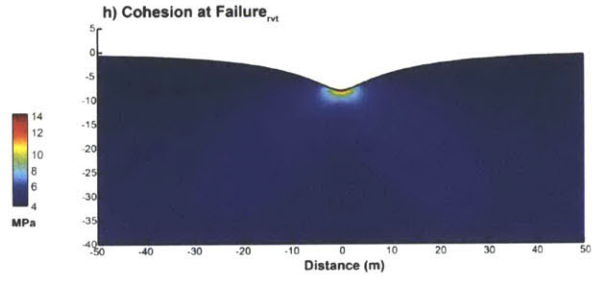
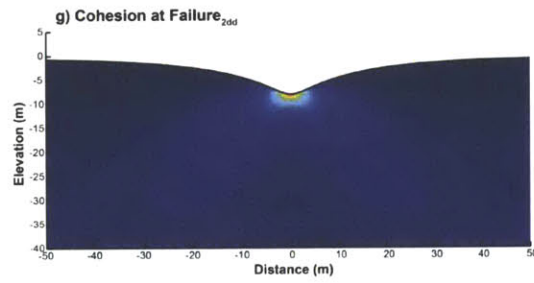
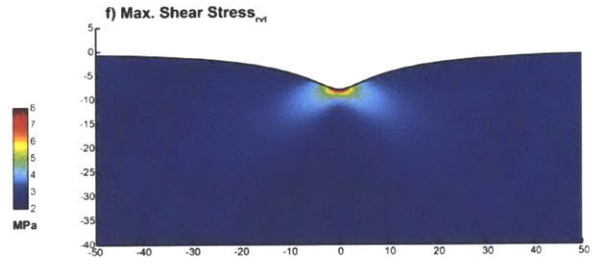
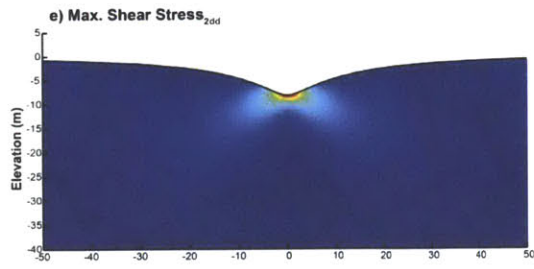


Figure A-2: Continued.

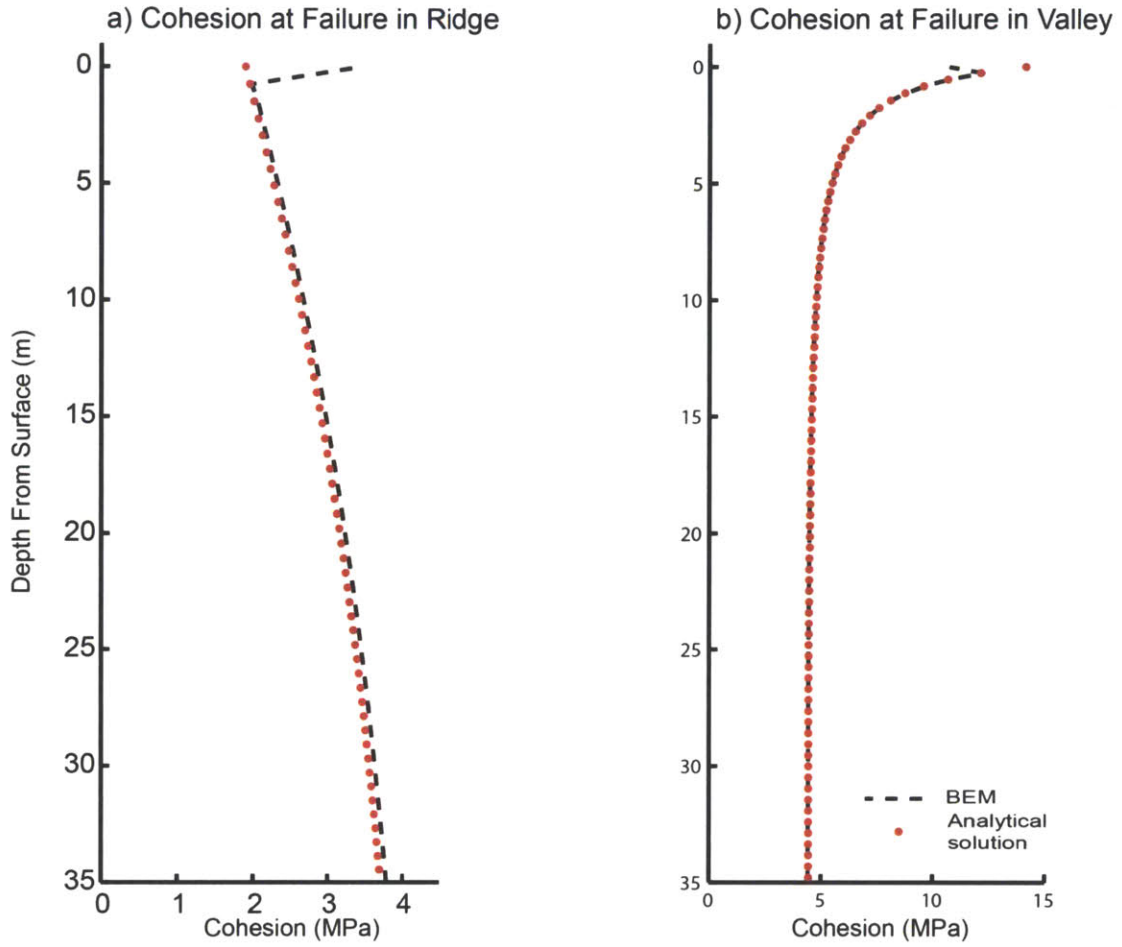
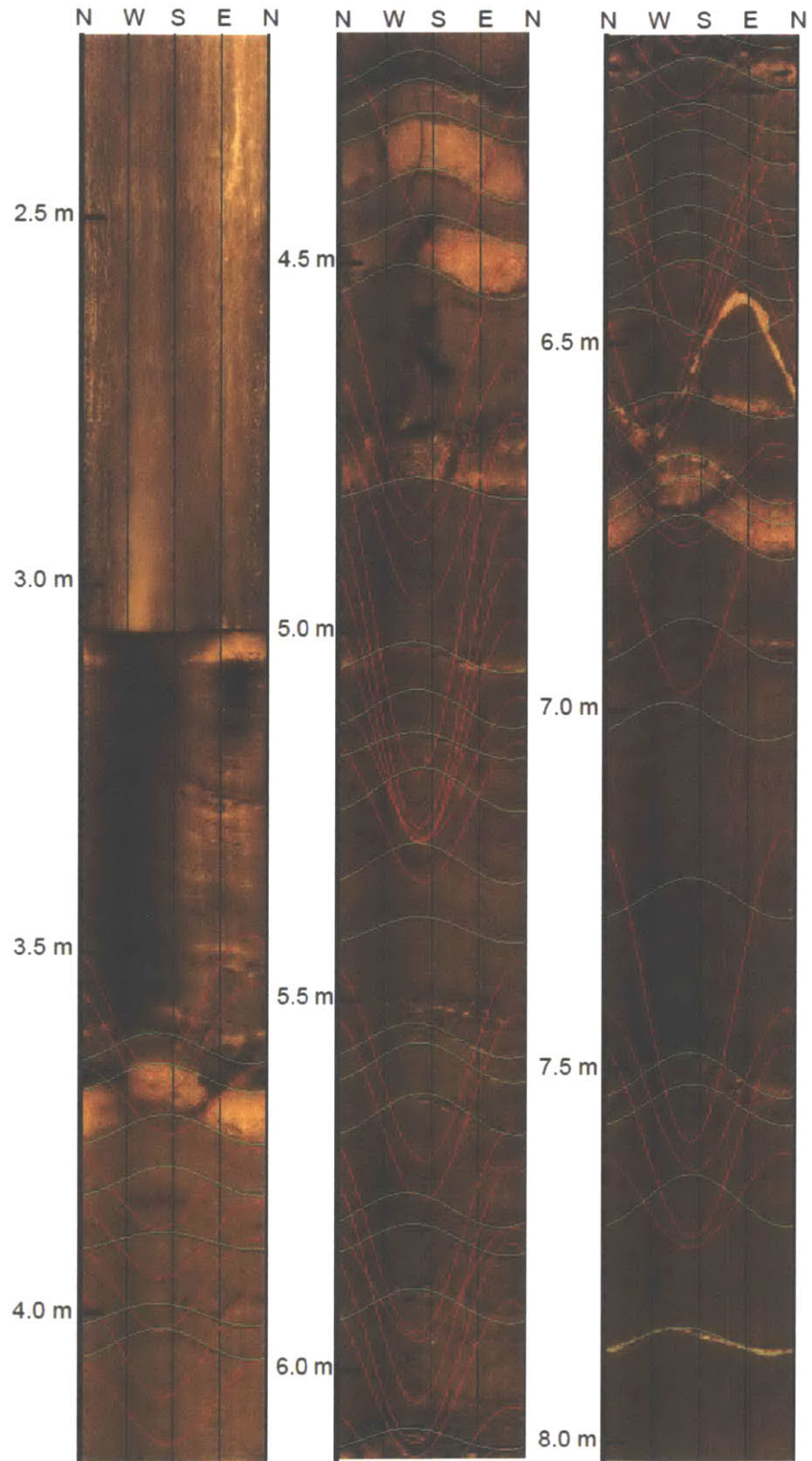
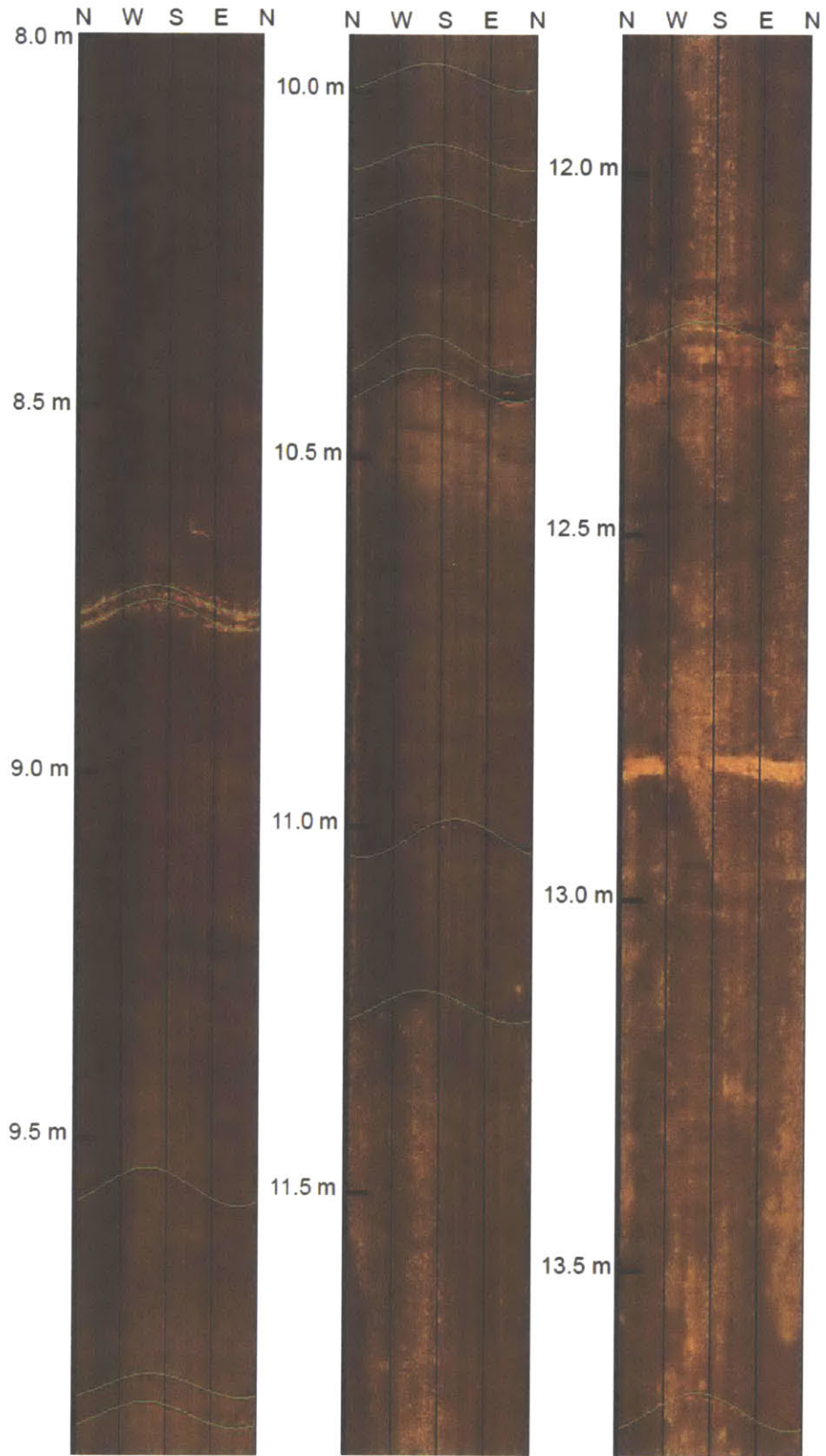


Figure A- 3: Cohesion-at-failure,  $C_{min}$ , under (a) the ridgetop in Figure A-1 and (b) the valley floor in Figure A-2 calculated with the BEM (2dd) and rvt methods. Curves are calculated with an internal friction angle,  $\phi$ , of  $24^\circ$ .

**Appendix B**  
**Borehole Image Logs and Structural Data**





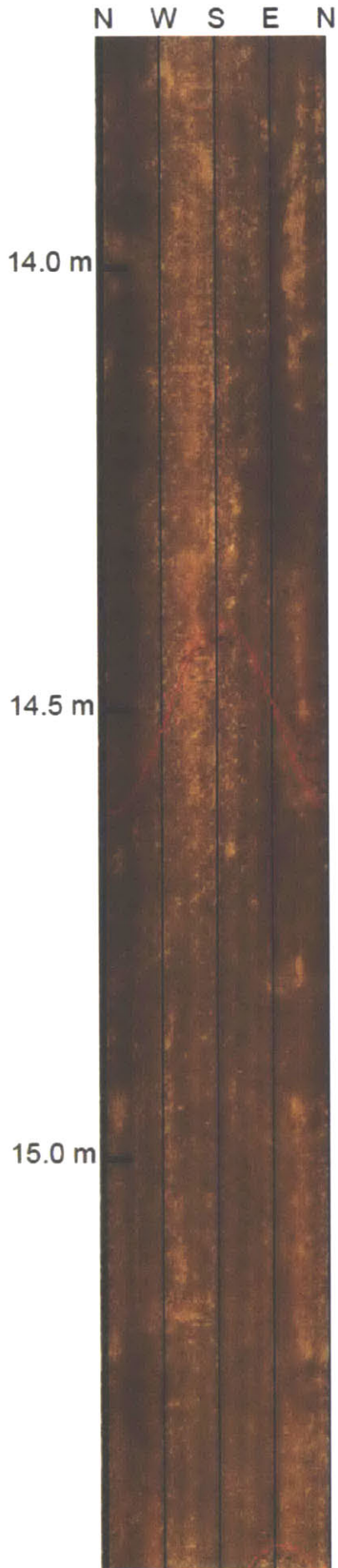
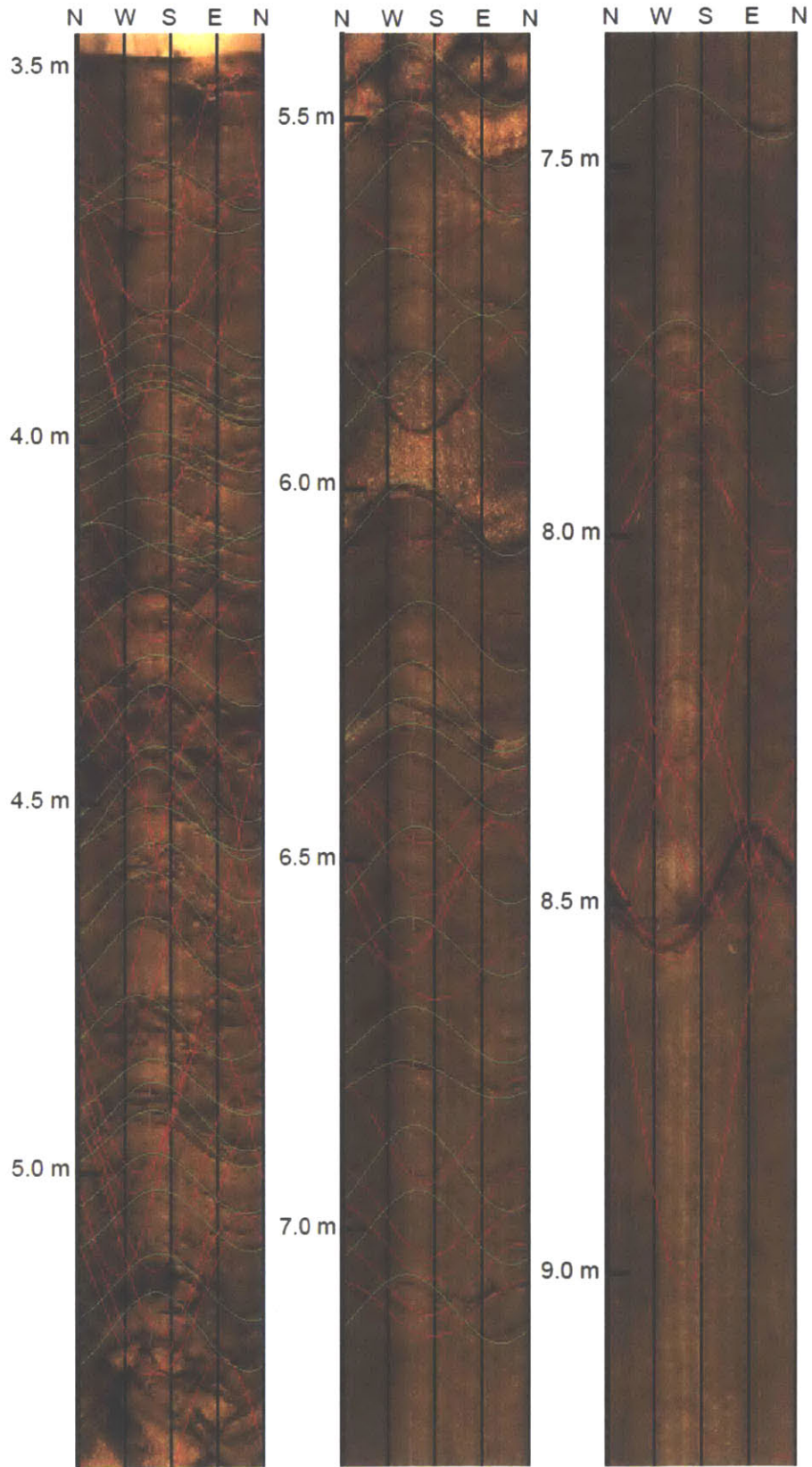


Figure B-1: Image log of CMZW 1 showing average traces (refer to text) of fracture (red) and bedding (green) planes.





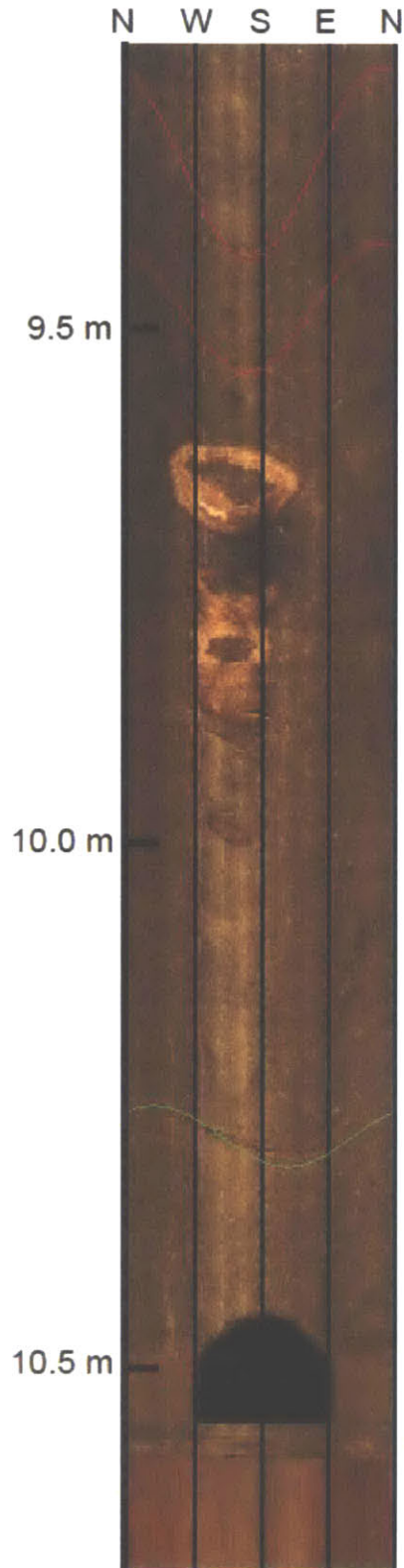
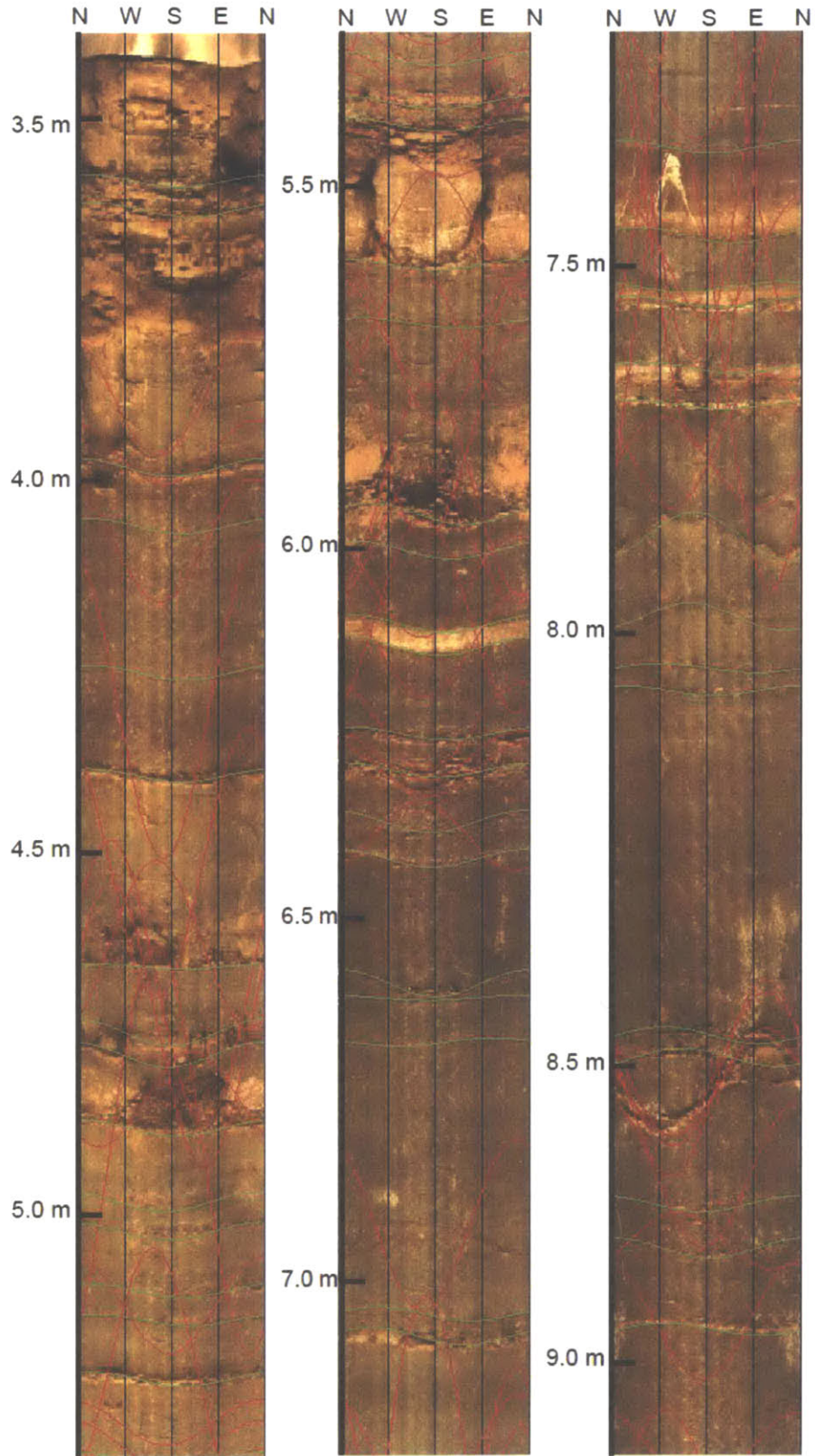
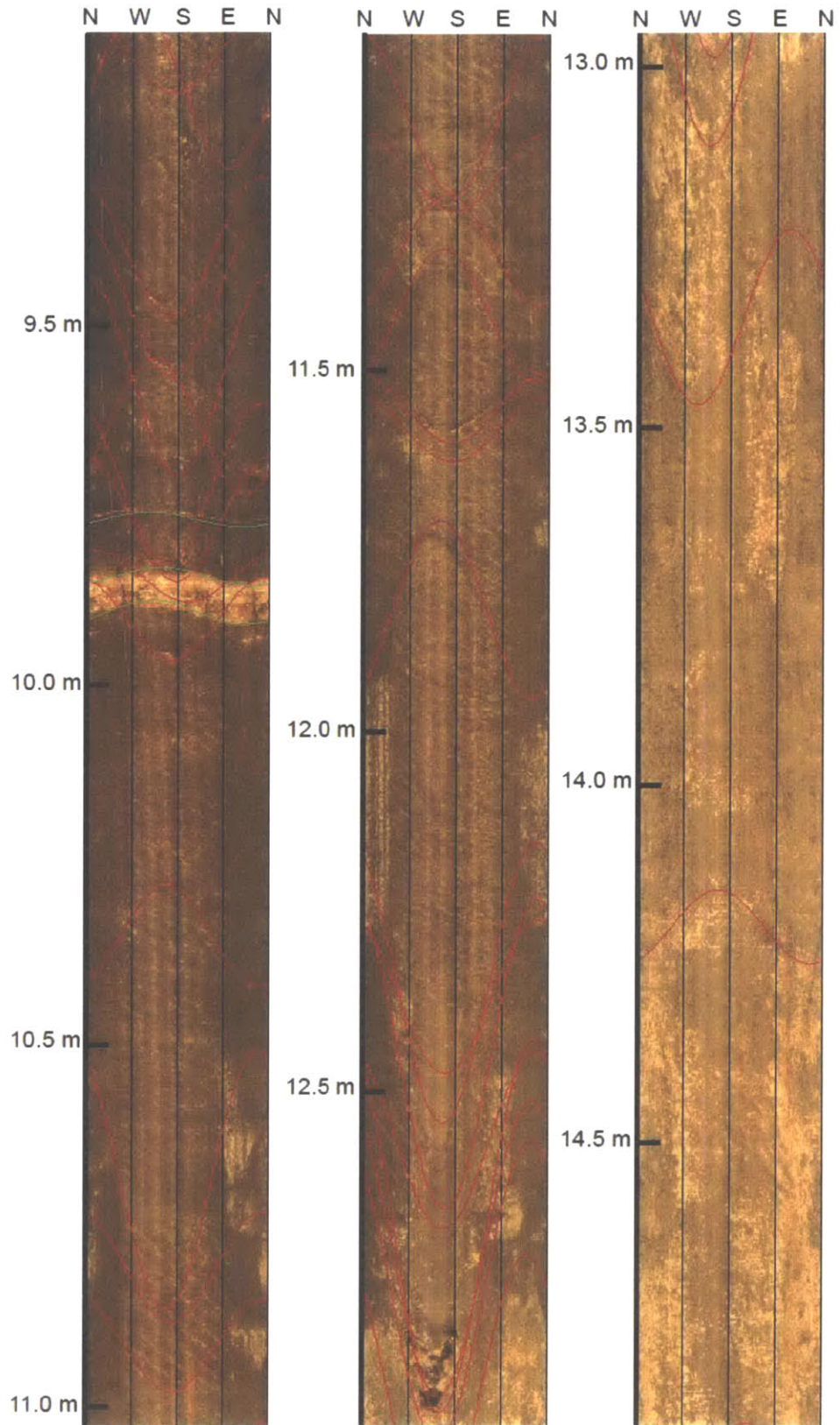


Figure B-2: Image log of CMZW 2 showing average traces (refer to text) of fracture (red) and bedding (green) planes





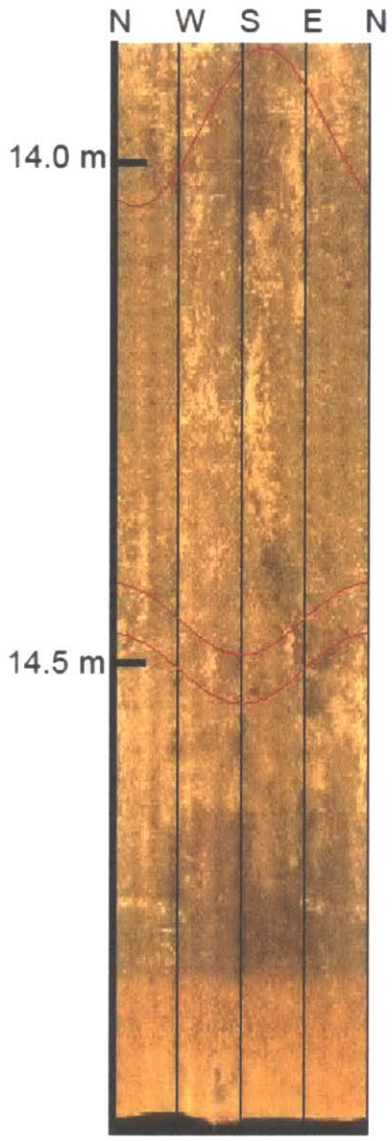
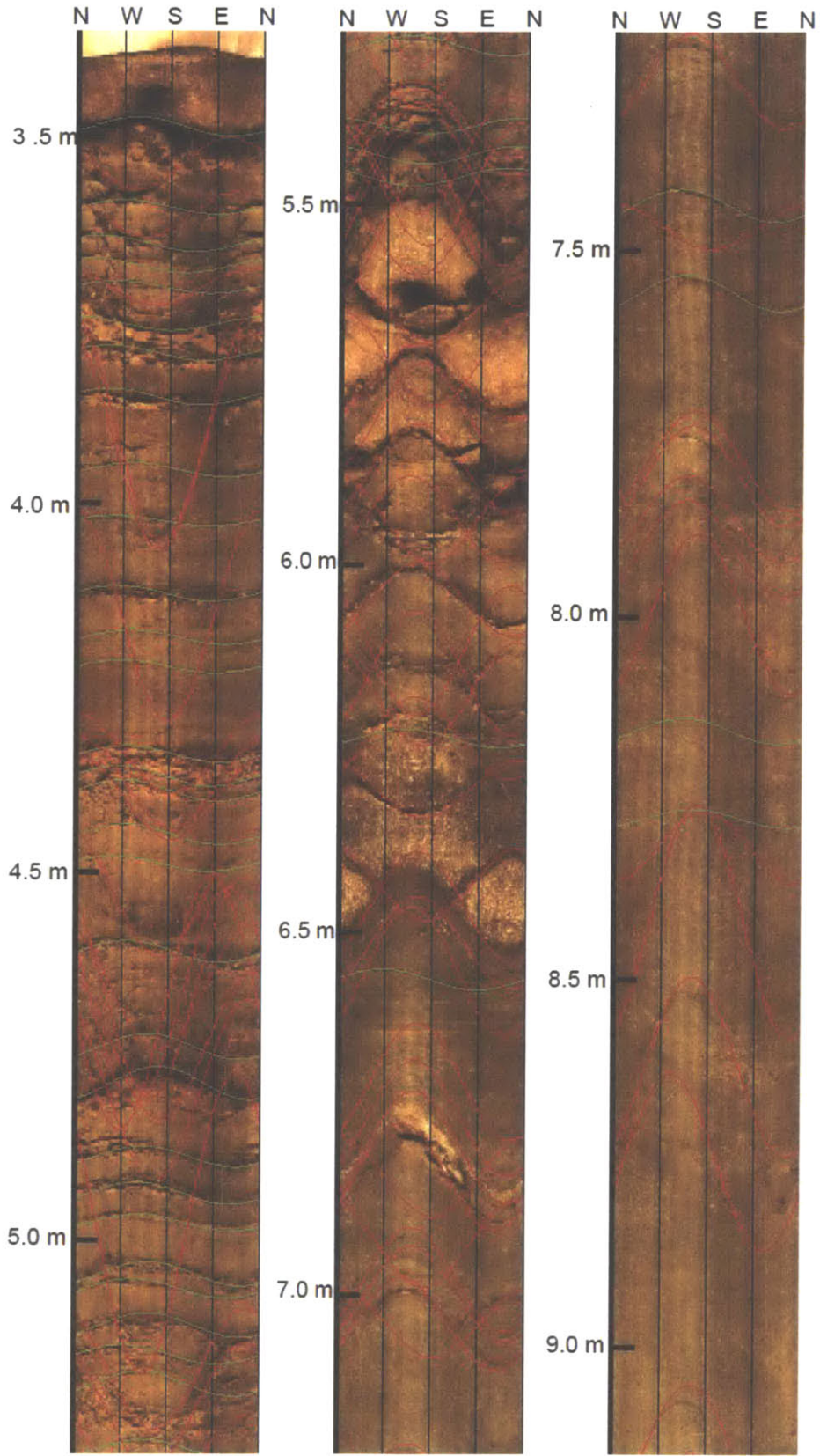
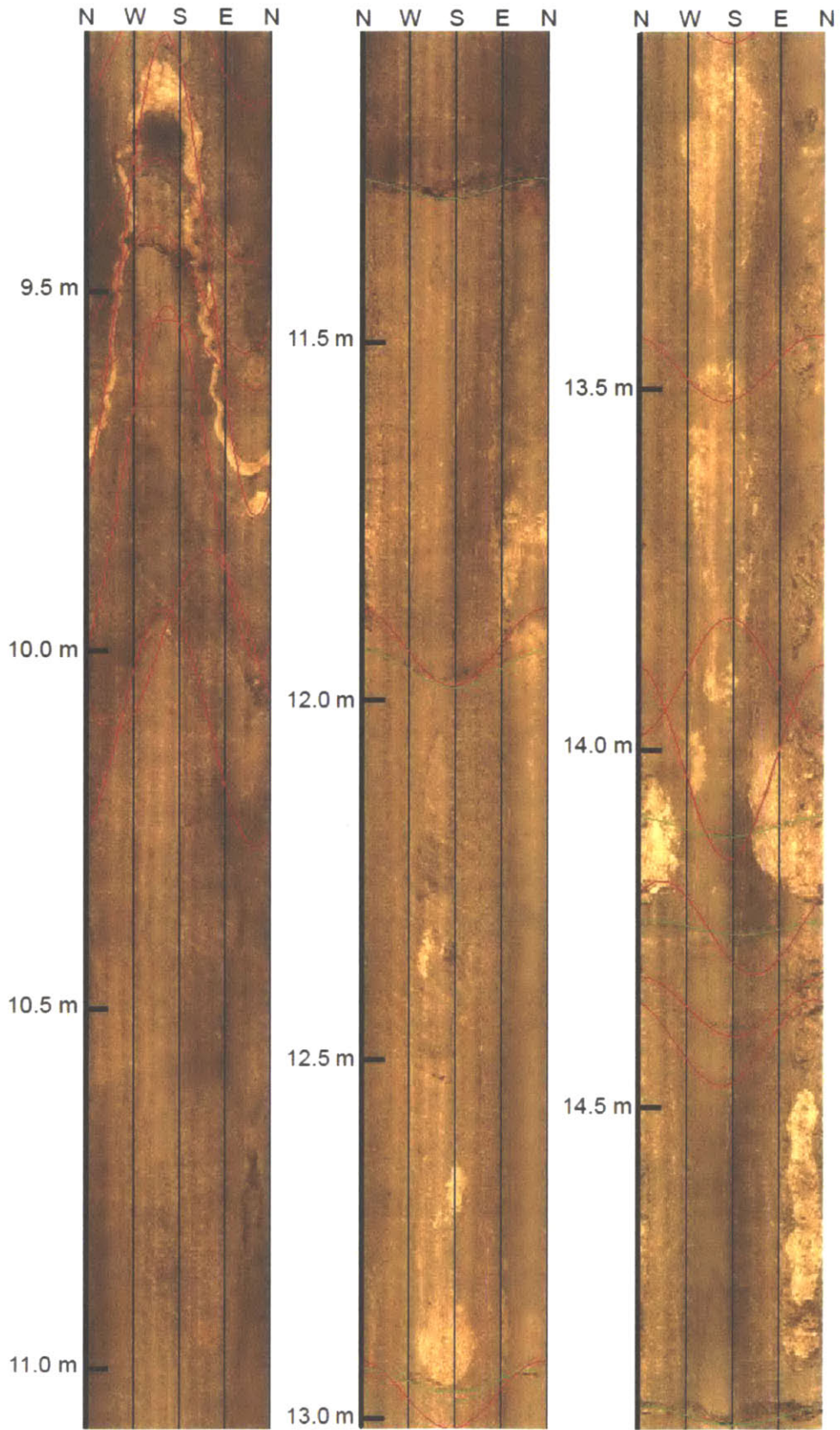


Figure B-3: Image log of CMZW 3 showing average traces (refer to text) of fracture (red) and bedding (green) planes.





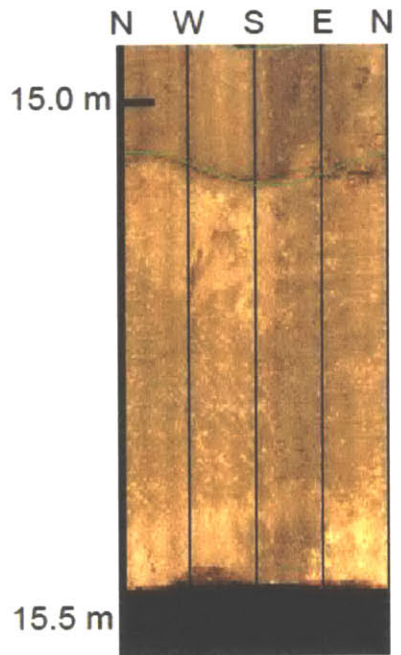


Figure B-4: Image log of CMZW 4 showing average traces (refer to text) of fracture (red) and bedding (green) planes.



Table B-1: CMZW 1 bedding plane strike directions and dip angles.

	<u>Depth</u> <u>(m)</u>	<u>Bedding</u> <u>Mean</u> <u>Azimuth</u> <u>(Deg)</u>	<u>Bedding</u> <u>Mean</u> <u>Strike</u> <u>(Deg)</u>	<u>Bedding</u> <u>Mean</u> <u>Dip</u> <u>(Deg)</u>		<u>Depth</u> <u>(m)</u>	<u>Bedding</u> <u>Mean</u> <u>Azimuth</u> <u>(Deg)</u>	<u>Bedding</u> <u>Mean</u> <u>Strike</u> <u>(Deg)</u>	<u>Bedding</u> <u>Mean</u> <u>Dip</u> <u>(Deg)</u>
1	3.13	327.36	237.36	22.59	31	5.79	343.58	253.58	25.99
2	3.17	333.08	243.08	21.02	32	5.83	336.76	246.76	22.57
3	3.24	345.36	255.36	22.28	33	5.87	328.99	238.99	27.00
4	3.31	345.94	255.94	21.64	34	5.91	338.17	248.17	29.43
5	3.39	338.38	248.38	13.58	35	5.97	225.16	135.16	23.26
6	3.49	328.77	238.77	17.11	36	6.08	311.38	221.38	19.84
7	3.53	332.67	242.67	22.99	37	6.18	330.86	240.86	34.08
8	3.72	332.63	242.63	27.13	38	6.21	332.37	242.37	32.23
9	3.76	335.12	245.12	28.26	39	6.26	330.75	240.75	32.21
10	3.8	350.08	260.08	21.93	40	6.4	339.18	249.18	30.95
11	3.88	347.72	257.72	25.99	41	6.51	302.39	212.39	27.60
12	3.94	355.24	265.24	23.16	42	6.75	339.94	249.94	28.64
13	4.01	310.40	220.40	26.02	43	6.99	339.52	249.52	31.52
14	4.29	331.69	241.69	16.48	44	7.03	344.45	254.45	29.19
15	4.52	320.75	230.75	22.61	45	7.16	345.15	255.15	35.08
16	4.59	330.48	240.48	27.89	46	7.35	326.04	236.04	19.85
17	4.64	329.34	239.34	19.80	47	8.26	331.98	241.98	22.13
18	4.7	341.08	251.08	31.01	48	8.28	331.21	241.21	22.58
19	4.8	330.62	240.62	28.73	49	9.06	321.88	231.88	27.62
20	4.89	335.94	245.94	19.60	50	9.33	329.55	239.55	18.10
21	5.04	325.65	235.65	25.67	51	9.37	320.00	230.00	20.09
22	5.07	335.77	245.77	28.89	52	9.48	332.91	242.91	20.62
23	5.14	342.82	252.82	29.69	53	9.59	342.00	252.00	20.07
24	5.27	313.06	223.06	25.03	54	9.66	337.61	247.61	17.89
25	5.31	324.76	234.76	23.30	55	9.86	320.24	230.24	29.14
26	5.4	330.21	240.21	25.28	56	9.9	323.53	233.53	24.91
27	5.58	319.86	229.86	16.62	57	10.52	28.71	298.71	27.55
28	5.63	349.03	259.03	24.37	58	10.75	326.39	236.39	23.87
29	5.69	343.38	253.38	21.65	59	11.73	334.73	244.73	20.27
30	5.73	336.44	246.44	25.21	60	13.2	333.83	243.83	27.09

Table B-2: CMZW 2 bedding plane strike directions and dip angles.

	<u>Depth</u> <u>(m)</u>	<u>Bedding</u> <u>Mean</u> <u>Azimuth</u> <u>(Deg)</u>	<u>Bedding</u> <u>Mean</u> <u>Strike</u> <u>(Deg)</u>	<u>Bedding</u> <u>Mean</u> <u>Dip</u> <u>(Deg)</u>		<u>Depth</u> <u>(m)</u>	<u>Bedding</u> <u>Mean</u> <u>Azimuth</u> <u>(Deg)</u>	<u>Bedding</u> <u>Mean</u> <u>Strike</u> <u>(Deg)</u>	<u>Bedding</u> <u>Mean</u> <u>Dip</u> <u>(Deg)</u>
1	3.16	334.27	244.27	32.98	27	4.56	334.87	244.87	39.93
2	3.20	288.21	198.21	25.76	28	4.65	337.37	247.37	42.31
3	3.36	352.82	262.82	32.43	29	4.71	330.93	240.93	46.70
4	3.39	343.86	253.86	30.78	30	4.94	313.11	223.11	40.58
5	3.42	333.76	243.76	29.51	31	5.02	304.05	214.05	41.71
6	3.45	334.66	244.66	28.50	32	5.08	332.89	242.89	45.38
7	3.46	340.05	250.05	28.33	33	5.22	283.30	193.30	42.53
8	3.52	331.97	241.97	27.81	34	5.32	89.92	359.92	47.89
9	3.55	332.88	242.88	28.26	35	5.37	333.66	243.66	47.88
10	3.61	305.39	215.39	29.15	36	5.54	320.24	230.24	45.93
11	3.65	216.26	126.26	26.29	37	5.70	336.54	246.54	43.53
12	3.68	341.79	251.79	27.54	38	5.78	320.67	230.67	47.91
13	3.74	322.92	232.92	35.30	39	5.82	311.68	221.68	36.72
14	3.83	333.67	243.67	35.11	40	5.85	317.14	227.14	32.42
15	3.89	338.94	248.94	47.67	41	5.90	317.88	227.88	40.37
16	3.97	332.39	242.39	45.59	42	6.02	325.35	235.35	46.46
17	4.01	323.15	233.15	51.34	43	6.12	311.39	221.39	38.59
18	4.03	326.29	236.29	31.54	44	6.25	317.55	227.55	37.34
19	4.09	333.48	243.48	39.61	45	6.30	305.05	215.05	27.28
20	4.14	317.93	227.93	45.60	46	6.42	323.14	233.14	49.36
21	4.20	318.23	228.23	44.87	47	6.51	327.24	237.24	45.16
22	4.30	295.90	205.90	41.11	48	6.61	306.52	216.52	42.92
23	4.37	327.66	237.66	37.25	49	6.93	315.24	225.24	36.34
24	4.42	328.53	238.53	42.89	50	7.26	318.74	228.74	45.21
25	4.45	327.51	237.51	37.87	51	9.78	215.81	125.81	30.41
26	4.51	326.19	236.19	39.07					

Table B-3: CMZW 3 bedding plane strike directions and dip angles.

	<u>Depth</u> <u>(m)</u>	<u>Bedding</u> <u>Mean</u> <u>Azimuth</u> <u>(Deg)</u>	<u>Bedding</u> <u>Mean</u> <u>Strike</u> <u>(Deg)</u>	<u>Bedding</u> <u>Mean</u> <u>Dip</u> <u>(Deg)</u>		<u>Depth</u> <u>(m)</u>	<u>Bedding</u> <u>Mean</u> <u>Azimuth</u> <u>(Deg)</u>	<u>Bedding</u> <u>Mean</u> <u>Strike</u> <u>(Deg)</u>	<u>Bedding</u> <u>Mean</u> <u>Dip</u> <u>(Deg)</u>
1	3.09	196.3	106.3	9.44	27	5.88	169.45	79.45	16.22
2	3.13	214.14	124.14	10.75	28	5.92	174.39	84.39	13.71
3	3.49	180.72	90.72	13.71	29	6.09	179.64	89.64	20.08
4	3.56	199.53	109.53	11.78	30	6.12	165.19	75.19	3.89
5	3.76	205.05	115.05	11.5	31	6.17	110.16	20.16	6.33
6	3.90	198.32	108.32	10.50	32	6.54	247.44	157.44	10.54
7	4.16	200.20	110.20	4.17	33	6.58	235.90	145.90	13.58
8	4.25	178.41	88.41	20.08	34	6.84	189.91	99.91	9.90
9	4.28	172.94	82.94	18.54	35	6.96	226.34	136.34	12.08
10	4.38	190.24	100.24	11.89	36	7.03	139.17	49.17	7.95
11	4.48	165.02	75.02	14.47	37	7.06	200.93	110.93	8.89
12	4.52	169.98	79.98	13.25	38	7.14	231.51	141.51	8.86
13	4.60	202.60	112.60	10.26	39	7.19	210.89	120.89	7.06
14	4.64	216.58	126.58	9.10	40	7.37	333.54	243.54	32.98
15	4.72	203.28	113.28	10.93	41	7.47	326.50	236.50	20.22
16	4.82	182.15	92.15	11.01	42	7.55	271.89	181.89	7.11
17	4.89	183.78	93.78	10.26	43	7.58	190.46	100.46	7.66
18	4.92	190.19	100.19	10.80	44	8.06	278.59	188.59	12.84
19	5.11	179.90	89.90	8.22	45	8.08	314.58	224.58	13.65
20	5.19	221.14	131.14	7.66	46	8.28	169.41	79.41	11.67
21	5.45	235.26	145.26	15.93	47	8.34	185.98	95.98	15.22
22	5.50	208.76	118.76	13.99	48	8.44	281.49	191.49	9.85
23	5.60	197.36	107.36	13.56	49	9.26	304.01	214.01	11.44
24	5.63	187.17	97.17	14.94	50	9.35	325.02	235.02	14.03
25	5.75	201.60	111.60	9.51	51	9.40	310.16	220.16	18.72
26	5.79	186.48	96.48	11.12					

Table B-4: CMZW 4 bedding plane strike directions and dip angles.

	<u>Depth</u> (m)	<u>Bedding</u> <u>Mean</u> <u>Azimuth</u> (Deg)	<u>Bedding</u> <u>Mean</u> <u>Strike</u> (Deg)	<u>Bedding</u> <u>Mean</u> <u>Dip</u> (Deg)		<u>Depth</u> (m)	<u>Bedding</u> <u>Mean</u> <u>Azimuth</u> (Deg)	<u>Bedding</u> <u>Mean</u> <u>Strike</u> (Deg)	<u>Bedding</u> <u>Mean</u> <u>Dip</u> (Deg)
1	2.98	296.48	206.48	14.31	24	4.48	303.60	213.60	12.90
2	3.09	268.65	178.65	10.84	25	4.55	321.16	231.16	18.48
3	3.14	225.80	135.80	12.34	26	4.57	292.90	202.90	14.86
4	3.16	207.43	117.43	11.40	27	4.62	320.59	230.59	18.27
5	3.19	254.57	164.57	9.46	28	4.66	276.12	186.12	14.69
6	3.26	179.37	89.37	10.62	29	4.70	307.74	217.74	18.68
7	3.29	243.19	153.19	12.04	30	4.79	315.46	225.46	15.13
8	3.36	241.06	151.06	12.59	31	4.90	167.43	77.43	11.92
9	3.45	288.50	198.50	11.10	32	4.94	158.44	68.44	13.58
10	3.52	254.86	164.86	7.89	33	4.98	138.16	48.16	13.27
11	3.62	259.22	169.22	11.93	34	5.74	306.78	216.78	13.91
12	3.68	286.36	196.36	11.27	35	6.06	265.60	175.60	15.88
13	3.72	268.58	178.58	9.88	36	6.94	302.25	212.25	24.52
14	3.84	276.27	186.27	12.85	37	7.06	313.20	223.20	26.72
15	3.86	261.96	171.96	15.70	38	7.66	309.61	219.61	19.34
16	3.89	271.85	181.85	15.99	39	7.78	328.14	238.14	14.12
17	3.95	277.47	187.47	15.26	40	10.79	161.16	71.16	15.62
18	3.98	255.58	165.58	12.22	41	11.45	178.62	88.62	27.50
19	4.11	277.35	187.35	16.65	42	12.45	175.05	85.05	19.24
20	4.24	319.44	229.44	19.50	43	13.61	169.11	79.11	15.46
21	4.29	339.95	249.95	24.29	44	13.75	195.29	105.29	10.80
22	4.38	311.91	221.91	15.54	45	14.43	186.10	96.10	14.79
23	4.44	300.33	210.33	16.80	46	14.56	199.07	109.07	18.34

Table B-5: CMZW 1 fracture plane strike directions and dip angles.

	<u>Depth</u> <u>(m)</u>	<u>Bedding</u> <u>Mean</u> <u>Azimuth</u> <u>(Deg)</u>	<u>Bedding</u> <u>Mean</u> <u>Strike</u> <u>(Deg)</u>	<u>Bedding</u> <u>Mean</u> <u>Dip</u> <u>(Deg)</u>		<u>Depth</u> <u>(m)</u>	<u>Bedding</u> <u>Mean</u> <u>Azimuth</u> <u>(Deg)</u>	<u>Bedding</u> <u>Mean</u> <u>Strike</u> <u>(Deg)</u>	<u>Bedding</u> <u>Mean</u> <u>Dip</u> <u>(Deg)</u>
1	3.07	142.30	52.30	61.58	22	5.34	153.86	63.86	72.60
2	3.12	152.20	62.20	56.99	23	5.37	157.11	67.11	57.03
3	3.19	175.45	85.45	42.55	24	5.44	150.34	60.34	69.77
4	3.33	153.20	63.20	47.40	25	5.49	151.42	61.42	64.58
5	3.39	156.98	66.98	45.01	26	5.60	154.62	64.62	51.65
6	3.46	154.20	64.20	50.77	27	5.64	144.87	54.87	43.01
7	3.53	162.39	72.39	55.02	28	5.82	157.67	67.67	73.12
8	3.62	170.10	80.10	47.98	29	5.86	139.45	49.45	32.45
9	3.86	197.74	107.74	67.66	30	5.88	148.57	58.57	70.01
10	4.14	148.79	58.79	73.92	31	5.98	87.40	357.40	72.73
11	4.23	150.74	60.74	67.90	32	6.04	85.86	355.86	67.31
12	4.30	158.54	68.54	68.88	33	6.13	147.09	57.09	44.73
13	4.43	151.86	61.86	78.13	34	6.19	144.43	54.43	49.38
14	4.47	156.15	66.15	77.22	35	6.20	148.93	58.93	50.69
15	4.51	156.72	66.72	75.53	36	6.31	149.84	59.84	69.18
16	4.60	157.22	67.22	71.65	37	6.88	162.66	72.66	76.64
17	4.68	166.96	76.96	62.47	38	7.01	170.20	80.20	65.46
18	4.72	163.46	73.46	62.30	39	7.09	164.52	74.52	69.01
19	5.07	165.69	75.69	69.61	40	7.18	162.05	72.05	52.17
20	5.13	164.60	74.60	68.49	41	14.01	7.99	277.99	65.25
21	5.27	152.16	62.16	70.07	42	15.01	100.80	10.80	51.71

Table B-6: CMZW 2 fracture plane strike directions and dip angles.

	<u>Depth</u> <u>(m)</u>	<u>Bedding</u> <u>Mean</u> <u>Azimuth</u> <u>(Deg)</u>	<u>Bedding</u> <u>Mean</u> <u>Strike</u> <u>(Deg)</u>	<u>Bedding</u> <u>Mean</u> <u>Dip</u> <u>(Deg)</u>		<u>Depth</u> <u>(m)</u>	<u>Bedding</u> <u>Mean</u> <u>Azimuth</u> <u>(Deg)</u>	<u>Bedding</u> <u>Mean</u> <u>Strike</u> <u>(Deg)</u>	<u>Bedding</u> <u>Mean</u> <u>Dip</u> <u>(Deg)</u>
1	3.07	142.51	52.51	48.81	28	5.36	167.59	77.59	55.52
2	3.10	146.66	56.66	48.42	29	5.51	159.55	69.55	48.53
3	3.18	151.53	61.53	33.20	30	5.91	159.27	69.27	45.64
4	3.21	150.22	60.22	28.13	31	5.99	169.59	79.59	54.72
5	3.24	102.34	12.34	77.92	32	6.02	134.84	44.84	59.42
6	3.27	156.09	66.09	63.62	33	6.03	114.08	24.08	63.24
7	3.29	162.93	72.93	41.70	34	6.14	183.96	93.96	40.34
8	3.36	140.28	50.28	60.43	35	6.37	167.07	77.07	55.02
9	3.47	160.76	70.76	72.36	36	6.46	172.86	82.86	50.31
10	3.63	141.63	51.63	61.81	37	6.51	175.01	85.01	45.09
11	3.71	155.96	65.96	47.70	38	6.58	169.81	79.81	43.60
12	3.77	157.51	67.51	57.46	39	6.60	175.53	85.53	36.92
13	3.83	91.06	1.06	62.73	40	7.22	150.13	60.13	47.91
14	3.86	156.41	66.41	57.56	41	7.27	155.47	65.47	37.84
15	3.96	155.72	65.72	45.30	42	7.37	336.89	246.89	58.39
16	4.04	227.78	137.78	74.07	43	7.45	324.95	234.95	65.23
17	4.09	57.87	327.87	76.35	44	7.47	328.72	238.72	52.86
18	4.18	69.07	339.07	69.38	45	7.67	147.21	57.21	72.17
19	4.37	116.96	26.96	68.19	46	7.83	328.97	238.97	72.13
20	4.39	104.58	14.58	70.82	47	7.88	257.60	167.60	70.44
21	4.46	77.38	347.38	72.86	48	7.90	214.65	124.65	66.33
22	4.46	146.26	56.26	68.61	49	7.94	346.40	256.40	73.73
23	4.55	164.00	74.00	70.36	50	7.97	110.28	20.28	59.45
24	4.64	154.14	64.14	64.76	51	7.99	120.86	30.86	60.55
25	4.65	131.74	41.74	65.06	52	8.26	149.79	59.79	79.15
26	4.92	97.89	7.89	70.98	53	8.85	163.12	73.12	61.57
27	5.16	159.40	69.40	33.71	54	8.98	160.66	70.66	51.21

Table B-7: CMZW 3 fracture plane strike directions and dip angles.

	<u>Depth</u> <u>(m)</u>	<u>Bedding</u> <u>Mean</u> <u>Azimuth</u> <u>(Deg)</u>	<u>Bedding</u> <u>Mean</u> <u>Strike</u> <u>(Deg)</u>	<u>Bedding</u> <u>Mean</u> <u>Dip</u> <u>(Deg)</u>		<u>Depth</u> <u>(m)</u>	<u>Bedding</u> <u>Mean</u> <u>Azimuth</u> <u>(Deg)</u>	<u>Bedding</u> <u>Mean</u> <u>Strike</u> <u>(Deg)</u>	<u>Bedding</u> <u>Mean</u> <u>Dip</u> <u>(Deg)</u>
1	3.39	154.48	64.48	59.22	42	8.07	112.29	22.29	62.90
2	3.45	164.45	74.45	41.04	43	8.09	111.04	21.04	69.49
3	3.57	157.04	67.04	59.28	44	8.10	113.13	23.13	57.92
4	3.78	164.65	74.65	76.78	45	8.13	111.81	21.81	53.37
5	3.99	149.51	59.51	74.79	46	8.22	172.76	82.76	63.21
6	4.15	330.15	240.15	66.39	47	8.33	304.21	214.21	37.56
7	4.21	241.50	151.50	75.41	48	8.43	171.38	81.38	57.67
8	4.24	242.86	152.86	75.50	49	8.62	169.08	79.08	48.28
9	4.34	39.20	309.20	52.17	50	8.65	279.41	189.41	65.85
10	4.38	330.21	240.21	79.73	51	8.89	162.93	72.93	62.69
11	4.62	175.20	85.20	52.59	52	8.96	165.74	75.74	65.72
12	4.72	323.28	233.28	74.22	53	9.06	177.51	87.51	70.40
13	4.78	169.43	79.43	31.56	54	9.15	311.98	221.98	62.29
14	4.80	169.36	79.36	33.70	55	9.22	158.16	68.16	65.93
15	4.84	172.00	82.00	33.86	56	9.27	175.98	85.98	60.07
16	4.89	188.06	98.06	40.58	57	9.33	198.63	108.63	35.34
17	4.92	183.73	93.73	43.33	58	9.41	168.58	78.58	48.93
18	4.96	204.67	114.67	32.28	59	9.86	337.07	247.07	54.34
19	5.07	353.16	263.16	59.58	60	10.20	156.98	66.98	74.47
20	5.18	164.18	74.18	56.01	61	10.31	167.88	77.88	56.92
21	5.21	321.39	231.39	62.26	62	10.42	168.55	78.55	51.82
22	5.21	184.62	94.62	64.78	63	10.63	171.42	81.42	65.99
23	5.30	159.35	69.35	71.01	64	10.72	175.20	85.20	47.81
24	5.43	344.18	254.18	70.82	65	10.83	339.54	249.54	57.11
25	5.45	337.74	247.74	61.51	66	10.92	331.02	241.02	61.44
26	5.55	152.84	62.84	54.17	67	11.04	170.99	80.99	44.53
27	5.61	335.51	245.51	69.25	68	11.08	170.93	80.93	41.64
28	5.63	159.55	69.55	54.97	69	11.31	327.06	237.06	67.96
29	5.74	164.87	74.87	50.07	70	11.86	154.71	64.71	75.63
30	5.78	160.54	70.54	33.90	71	11.88	159.22	69.22	64.84
31	5.80	165.65	75.65	35.02	72	11.96	158.58	68.58	76.93
32	5.89	331.56	241.56	43.20	73	12.07	155.70	65.70	67.86
33	6.41	155.21	65.21	66.77	74	12.19	149.95	59.95	79.02
34	6.72	158.84	68.84	60.89	75	12.25	147.72	57.72	76.29
35	6.79	342.57	252.57	80.01	76	12.32	145.56	55.56	76.48
36	6.82	154.09	64.09	79.03	77	12.44	139.00	49.00	75.37
37	6.97	161.95	71.95	79.81	78	12.84	114.62	24.62	67.73
38	6.99	185.53	95.53	59.70	79	13.71	336.31	246.31	45.73
39	7.11	300.98	210.98	80.67	80	14.49	30.60	300.60	57.64
40	7.23	111.18	21.18	61.33	81	14.96	179.67	89.67	35.88
41	7.27	275.78	185.78	50.82	82	15.01	180.01	90.01	34.89

Table B-8: CMZW 4 fracture plane strike directions and dip angles.

	<u>Depth</u> <u>(m)</u>	<u>Bedding</u> <u>Mean</u> <u>Azimuth</u> <u>(Deg)</u>	<u>Bedding</u> <u>Mean</u> <u>Strike</u> <u>(Deg)</u>	<u>Bedding</u> <u>Mean</u> <u>Dip</u> <u>(Deg)</u>		<u>Depth</u> <u>(m)</u>	<u>Bedding</u> <u>Mean</u> <u>Azimuth</u> <u>(Deg)</u>	<u>Bedding</u> <u>Mean</u> <u>Strike</u> <u>(Deg)</u>	<u>Bedding</u> <u>Mean</u> <u>Dip</u> <u>(Deg)</u>
1	3.04	113.54	23.54	35.58	42	5.94	166.54	76.54	44.82
2	3.10	129.38	39.38	31.92	43	5.97	332.19	242.19	56.05
3	3.21	150.50	60.50	26.95	44	6.01	333.10	243.10	51.32
4	3.39	162.65	72.65	72.43	45	6.06	321.07	231.07	60.47
5	3.44	159.36	69.36	71.44	46	6.21	331.46	241.46	58.20
6	3.64	176.12	86.12	70.90	47	6.26	327.08	237.08	57.66
7	3.85	183.43	93.43	47.09	48	6.31	326.37	236.37	56.97
8	3.88	186.02	96.02	51.30	49	6.34	302.19	212.19	55.70
9	3.91	183.88	93.88	48.72	50	6.35	183.12	93.12	47.03
10	4.02	163.11	73.11	60.49	51	6.42	167.15	77.15	50.29
11	4.16	159.78	69.78	59.62	52	6.48	321.34	231.34	54.75
12	4.16	145.02	55.02	71.62	53	6.51	323.78	233.78	52.50
13	4.16	117.33	27.33	71.32	54	6.54	186.49	96.49	42.95
14	4.19	85.47	355.47	73.86	55	6.54	305.03	215.03	51.27
15	4.24	163.81	73.81	63.18	56	6.76	319.44	229.44	52.62
16	4.30	153.77	63.77	67.75	57	6.97	178.60	88.60	30.72
17	4.47	131.48	41.48	76.28	58	7.27	331.53	241.53	53.67
18	4.67	154.79	64.79	58.99	59	7.30	326.83	236.83	53.79
19	4.73	149.76	59.76	59.55	60	7.35	316.61	226.61	50.11
20	4.81	149.53	59.53	52.41	61	7.40	318.13	228.13	52.86
21	4.88	324.04	234.04	46.34	62	7.49	336.70	246.70	65.65
22	4.91	328.48	238.48	49.92	63	7.81	351.58	261.58	44.41
23	4.92	146.91	56.91	58.17	64	7.92	337.76	247.76	72.63
24	4.95	329.99	239.99	58.66	65	8.11	329.32	239.32	67.89
25	4.97	164.90	74.90	59.23	66	8.25	289.28	199.28	67.40
26	5.01	309.64	219.64	61.40	67	8.66	327.49	237.49	62.44
27	5.03	147.01	57.01	52.39	68	8.90	313.38	223.38	55.23
28	5.06	335.43	245.43	59.86	69	8.99	330.39	240.39	81.46
29	5.14	173.81	83.81	42.12	70	9.01	308.36	218.36	60.11
30	5.23	178.93	88.93	52.65	71	9.09	331.61	241.61	44.24
31	5.25	330.69	240.69	46.23	72	9.28	334.27	244.27	78.63
32	5.29	339.22	249.22	56.13	73	9.47	53.08	323.08	68.32
33	5.37	330.16	240.16	50.66	74	9.62	330.90	240.90	73.17
34	5.44	176.12	86.12	49.79	75	11.43	174.15	84.15	47.24
35	5.44	314.20	224.20	49.83	76	12.46	172.24	82.24	43.57
36	5.55	329.76	239.76	44.77	77	12.97	161.02	71.02	42.91
37	5.61	148.93	58.93	60.39	78	13.41	352.93	262.93	58.69
38	5.64	328.35	238.35	59.69	79	13.52	171.13	81.13	69.78
39	5.67	160.44	70.44	54.58	80	13.75	221.35	131.35	52.54
40	5.75	326.04	236.04	48.38	81	13.84	180.06	90.06	39.71
41	5.81	161.80	71.80	37.75	82	13.91	157.69	67.69	49.99



## References

- Augustinus, P.C., 1995. Glacial valley cross-profile development: the influence of in situ rock stress and rock mass strength, with examples from the Southern Alps, New Zealand. *Geomorphology*. **14**: 87-97. DOI: 10.1016/0169-555X(95)00050-X.
- Clarke, B.A., and Burbank, D.W., 2011. Quantifying bedrock-fracture patterns within the shallow subsurface: Implications for rock mass strength, bedrock landslides, and erodibility. *Journal of Geophysical Research*. **116**: F04009. DOI: 10.1029/2011JF001987.
- Crouch, S.L., and Starfield, A.M., 1983. *Boundary element methods in solid mechanics*. Allen and Unwin Ltd.: UK.
- Dühnforth, M., Anderson, R.S., Ward, D., and Stock, G.M., 2010. Bedrock fracture control of glacial erosion processes and rates. *Geology*. **38**: No. 5. 423-426. DOI: 10.1130/G30576.1.
- Heidbach, O., Tingay, M., Barth, A., Reinecker, J., Kurfeß, D., and Müller, B., The World Stress Map database release 2008 doi:10.1594/GFZ.WSM.Rel2008, 2008.
- Holzhausen, G.R., 1978. Sheet structure in rock and some related problems in rock mechanics. PhD dissertation. Department of Applied Earth Sciences, Stanford University: Stanford, California.
- Jaeger, J.C., Cook, N.G.W., and Zimmerman, R. W., 2007. *Fundamentals of rock mechanics* (4<sup>th</sup> ed.). Blackwell Publishing Ltd.: USA.
- Jin, L., Ravella, R., Ketchum, B., Bierman, P.R., Heaney, P., White, T., and Brantley, S.L., 2010. Mineral weathering and elemental transport during hillslope evolution at the Susquehanna/Shale Hills Critical Zone Observatory. *Geochimica et Cosmochimica Acta* **74**: 3669-3691.
- Kuntz, B., Rubin, S., Berkowitz, B., and Singha, K., 2011. Quantifying solute transport behavior at the Shale Hills Critical Zone Observatory. *Vadose Zone Journal* **10**: 843-857. DOI:10.2136/vzj2010.0130.
- Luthi, S.M., 2001. *Geological well logs: use in reservoir modeling*. Springer-Verlag: Berlin.
- Lynch, J.A., 1976. Effects of antecedent soil moisture on storm hydrographs. PhD Dissertation. Pennsylvania State University: University Park, Pennsylvania.
- Martel, S.J., 2000. Modeling elastic stresses in long ridges with the displacement discontinuity method. *Pure and Applied Geophysics* **157**: 1039-1057.

- Martel, S.J., 2011. Mechanics of curved surfaces, with application to surface-parallel cracks. *Geophysical Research Letters* **30**: L20303. DOI: 10.1029/2011GL049354.
- Martel, S.J., and Muller, J.R., 2000. A two-dimensional boundary element method for calculating elastic gravitational stresses in slopes. *Pure and Applied Geophysics* **157**: 989-1007.
- McNutt, M., 1980. Implications of regional gravity for state stress in the earth's crust and upper mantle. *Journal of Geophysical Research* **85**: B11, 6377-6396.
- McTigue, D.F., and Mei, C.C., 1981. Gravity-induced stresses near topography of small slope. *Journal of Geophysical Research* **86**: B10, 9268-9278.
- Miller, D.J., and Dunne, T., 1996. Topographic perturbations of regional stresses and consequent bedrock fracturing. *Journal of Geophysical Research* **101**: B11, 25,523-25,536.
- Molnar, P., 2004. Interactions among topographically induced elastic stress, static fatigue, and valley incision. *Journal of Geophysical Research* **109**: F02010. DOI: 10.1029/2003JF000097.
- Moore, J.R., Sanders, J.W., Dietrich, W.E., and Glaser, S.D., 2009. Influence of rock mass strength on the erosion rate of alpine cliffs. *Earth Surface Processes and Landforms* **34**: 1339-1352. DOI: 10.1002/esp.1821.
- Morin, R.H., and Savage, W.Z., 2002. Topographic stress perturbations in southern Davis Mountains, west Texas, 2, Hydrogeologic implications. *Journal of Geophysical Research* **107**: B12, 2340. DOI: 10.1029/2001JB000488.
- Morin, R.H., Savage, W.Z., and Rivard, C., 2006. Hydrologic consequences of gravity-induced stresses along a ridge - example from Annapolis Valley, Nova Scotia: Proceedings, 41st U.S. Symposium on Rock Mechanics, June 17-21. American Rock Mechanics Association, paper no. 1054: Golden, Colorado.
- Muskhelishvili, N.I., 1953. Some basic problems of the mathematical theory of elasticity (4<sup>th</sup> ed.). P. Noordhoff Ltd.: The Netherlands.
- Plumb, R.A., and Cox, J.W., 1987. Stress directions in eastern north America determined to 4.5 Km from borehole elongation measurements. *Journal of Geophysical Research* **92**: B6, 4805-4816.
- Savage, W.Z., Swolfs, H.S., and Powers, P.S., 1985. Gravitational stresses in long symmetric ridges and valleys. *International Journal of Rock Mechanics and Mining Sciences and Geomechanics Abstracts* **22**: No. 5, 291-302.
- Savage, W.Z., and Swolfs, H.S., 1986. Tectonic and gravitational stress in long symmetric ridges and valleys. *Journal of Geophysical Research* **91**: 3677-3685.

- Savage, W.Z., and Morin, R.H., 2002. Topographic stress perturbations in southern Davis Mountains, west Texas, 1, Polarity reversal of principal stresses. *Journal of Geophysical Research* **107**: B12, 2339. DOI: 10.1029/2001JB000484.
- Serra, O., 1989. Formation MicroScanner image interpretation. Schlumberger Educational Services: Houston, Texas.
- Singha, K., White, T., and Perron J. T., 2012. Fracture patterns and their relations to groundwater flow within the Shale Hills Critical Zone Observatory. Unpublished manuscript.
- Sneddon, I.N., 1951. Fourier Transform. McGraw-Hill: New York.
- Zoback, M.L., and Zoback, M.D., 1980. State of stress in the conterminous United States. *Journal of Geophysical Research* **85**: B11, 6113-6156.
- Zoback, M.L., and Zoback, M.D., 1989. Tectonic stress fields of the continental United States. In *Geophysical framework of the continental United States*, Pakiser, L.C., and Mooney, W.D. (eds). Geological Society of America Memoir 172: Boulder, Colorado.
- Zoback, M. D., 2007. Reservoir Geomechanics. Cambridge University Press: UK.